

# Sparse, self-organizing ensembles of local kernels detect rare statistical anomalies

Gaia Grosso<sup>a,b,c</sup>, Sai Sumedh R. Hindupur<sup>c</sup>, Thomas Fel<sup>c,d</sup>,  
Samuel Bright-Thonney<sup>a,b</sup>, Philip Harris<sup>a,b</sup>, and Demba Ba<sup>c,d</sup>

## Abstract

Modern artificial intelligence has revolutionized our ability to extract rich and versatile data representations across scientific disciplines. Yet, the statistical properties of these representations remain poorly controlled, causing misspecified anomaly detection (AD) methods to falter. Weak or rare signals can remain hidden within the apparent regularity of normal data, creating a gap in our ability to detect and interpret anomalies. We examine this gap and identify a set of structural desiderata for detection methods operating under minimal prior information: *sparsity*, to enforce parsimony; *locality*, to preserve geometric sensitivity; and *competition*, to promote efficient allocation of model capacity. These principles define a class of self-organizing local kernels that adaptively partition the representation space around regions of statistical imbalance. As an instantiation of these principles, we introduce SPARKER, a sparse ensemble of Gaussian kernels trained within a semi-supervised Neyman–Pearson framework to locally model the likelihood ratio between a sample that may contain anomalies and a nominal, anomaly-free reference. We provide theoretical insights into the mechanisms that drive detection and self-organization in the proposed model, and demonstrate the effectiveness of this approach on realistic high-dimensional problems of scientific discovery, open-world novelty detection, intrusion detection, and generative-model validation. Our applications span both the natural- and computer-science domains. We demonstrate that ensembles containing only a handful of kernels can identify statistically significant anomalous locations within representation spaces of thousands of dimensions, underscoring both the interpretability, efficiency and scalability of the proposed approach.

## Index Terms

anomaly detection, interpretability, likelihood-ratio, goodness-of-fit

## I. INTRODUCTION

Finding data patterns that do not conform to nominal behavior, a practice that goes under the name of anomaly detection (AD) [1], plays a central role in the scientific method, enabling the discovery of novel phenomena and advancing our understanding of the natural world [2-7]. Based on theories and controlled experiments, scientists construct generative models of observed phenomena, and hope to reveal new laws of nature as unexpected deviations. Similarly, AD is at the core of data quality monitoring, validation and control tools, enabling a safe interaction with the myriad of artificial systems that surround us [8-10]. AD also addresses the growing need in computer science for robust methods to test, interpret, and align generative models, a challenge made urgent by the advent of unprecedentedly large models in vision and language [11-13].

AD is a challenging problem for two key reasons: (1) the variety of ways anomalies manifest in data (e.g. in-distribution, out-of-distribution, point-like, collective, ...) and, more often than not, (2) the dearth of information about the time and location of their occurrence [1]. Several methods exist to tackle different AD settings [14]. Broadly speaking, if the fraction of anomalous points in a dataset is large, key properties about the signal can be learned from the data by means of arbitrarily flexible models, whereas in anomaly-scarce regimes the lack of evidence must be replaced by inductive bias [15]. Feature engineering, geometry, smoothness are just a few examples of design choices that implicitly shape models for AD. The performance of AD tools is thus tightly intertwined with the correctness of the modeling assumptions they rely on [16], [17].

Concurrent with the growing need for robust AD tools, advances in representation learning have revolutionized data analysis across scientific and technological domains, enabling scalable statistical inference on massive datasets and complex high-dimensional problems [18-21].

In spite of this, the statistical properties of neural embeddings remain poorly controlled, exposing downstream AD to failure modes when the anomalies do not behave as expected. As depicted in panel (a) of Figure 1, most contemporary AD methods rely on assumptions of separability or dense supervision that break down when anomalies are rare, weakly expressed, or embedded within the data manifold [22-25], leaving this corner of the anomaly space unexplored.

We address this gap by introducing an AD method for *in-distribution* anomalies, arising as subtle over- or under-densities that locally distort the nominal data distribution. Motivated by applications across natural and computer sciences, we propose three principled desiderata for AD algorithms —*sparsity*, *locality*, and *competition*—as fundamental to discovering and characterizing

<sup>a</sup>NSF AI Institute for Artificial Intelligence and Fundamental Interactions, Cambridge, 02139, MA

<sup>b</sup>Laboratory for Nuclear Science, Massachusetts Institute of Technology, Cambridge, 02139, MA

<sup>c</sup>School of Engineering and Applied Sciences, Harvard University, Allston, 02134, MA

<sup>d</sup>Kempner Institute for the Study of Natural and Artificial Intelligence, Harvard University, Allston, 02134, MA

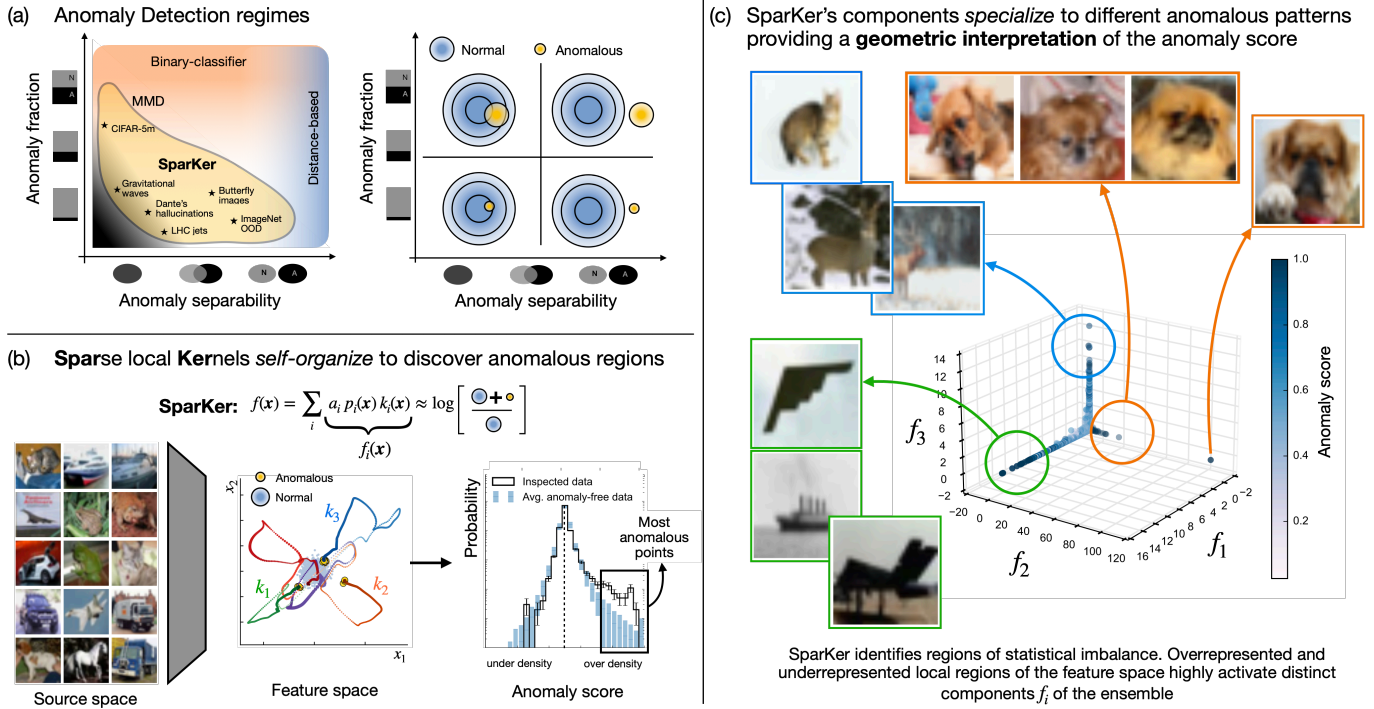


**Fig. 1: Detecting rare in-distribution anomalies with SPARKER.** (a) Cartoon diagram illustrating the regimes of anomaly detection; problems are characterized by anomaly separability ( $x$ -axis) and anomaly fraction ( $y$ -axis). Detection becomes harder near the origin, where anomalies are rare and overlap with normal data. The right panel qualitatively pictures the different corners of the space. The left panels highlights the region SPARKER. is designed for, e.g. low anomaly fraction and separability. The stars indicate the suite of applications from natural and computer science that we showcase in Sections IV and V. (b) SparKer’s anomaly detection pipeline: source data are embedded to extract domain-specific features; SPARKER. compares the distribution of the inspected data to anomaly-free data in feature space by means of a self-organizing ensemble of local kernels, and extracts an *anomaly score*; (c) Sparsity, locality and competition, which underlie the SPARKER. model, make it possible to decompose the anomaly score into distinct, interpretable components,  $\{f_i\}$ , pointing at different anomalous regions in the feature space, thus enabling a geometry-aware analysis of the anomalies.

novel patterns in latent representations. These principles motivate the design of efficient ensembles of local kernels that self-organize around anomalous regions in high-dimensional spaces while retaining interpretability. As a concrete realization, we introduce SparKer, a sparse ensemble of Gaussian kernels equipped with a competition mechanism. Panel (b) of Figure 1 shows how SPARKER. operates in feature space. SparKer’s self-organizing Gaussian kernels model the log-density ratio between the inspected data (a mixture of anomalous and normal occurrences) and an anomaly-free reference set, yielding an interpretable anomaly score.

We demonstrate the effectiveness of this framework across diverse applications—from scientific discovery to generative model validation, novelty detection, and intrusion detection—spanning multiple data modalities, dimensionalities, and scientific domains. Remarkably, ensembles containing only a handful of kernels can identify statistically significant anomalous regions within representation spaces of thousands of dimensions. Panel (c) of Figure 1 illustrates SparKer’s ability to characterize anomalous regions: the sparse kernel components provide low-dimensional representations that isolate the most anomalous regions of the data (dark blue points), revealing distinct underlying anomaly types.

Taken together, our findings demonstrate that *sparsity*, *locality*, and *competition* are key properties for building *scalable* and *interpretable* AD models, opening new frontiers in scientific discovery, monitoring, and validation of natural and artificial systems.

The rest of our treatment begins in Section II, where we introduce SPARKER. and the design principles behind it. In Section III, we analyze the detection properties and training dynamics of the model in a teacher/student setting, providing theoretical and numerical insights in support of its design principles. In Section IV, we show the performance of SPARKER. on AD problems spanning scientific discovery, generative AI validation, novelty and intrusion detection. In Section V we provide guidelines for interpreting the detected anomalies, and discuss domain-specific, actionable findings from the various applications considered in Section IV. Finally, in Section VI we conclude and suggest future research directions.

## II. SPARSE ENSEMBLES OF LOCAL KERNELS (SPARKER)

### A. Anomaly detection regimes

In AD, different problem settings require different assumptions on the anomaly [26]. In the absence of a priori knowledge about the signal, two parameters strongly characterize AD problems: (1) the amount of information about the signal hidden in the inspected data (i.e. anomaly fraction), and (2) how difficult it is to distinguish between anomalous and normal data in representation space (i.e. anomaly separability)<sup>1</sup>. The former shapes the balance between expressivity and inductive bias in model design; the latter guides the choice of the statistical method to employ. Panel (a) of Figure 1 gives a qualitative view of the most appropriate AD methods given the problem setting: for large anomaly fractions, binary classifiers with standard methods of regularization are the most practical way to learn a density ratio and solve the AD problem [27-29]; on the other hand, if the signal is known to lay in the extreme tails of the distribution of anomaly-free data, then distance-based methods, neglecting distribution shape, are more suitable candidates [30-32]. We focus on the challenging scenario where the anomaly fraction is low and separability is not guaranteed (bottom left corner of the diagram), and show that a Neyman-Pearson approach to hypothesis testing [33] coupled with a proper set of inductive biases lead to sensitivity in these regimes.

### B. Neyman-Pearson two-sample test

The Neyman-Pearson (NP) test addresses the problem of statistical anomaly detection by performing a signal-agnostic two-sample test based on the ratio of likelihoods [26], [33-35]. Given a dataset  $\mathcal{D}$  comprising  $N_{\mathcal{D}}$  statistically independent unlabeled observations, and a reference sample  $\mathcal{R}$  of size  $N_{\mathcal{R}}$  distributed according to the nominal data condition  $H_0$ , we quantify the degree of compatibility between the data and the assumed reference model with a likelihood-ratio test

$$t_{\text{NP}}(\mathcal{D}) = 2 \max_{\theta} \left[ \log \frac{\mathcal{L}(\mathcal{D}|H_{\theta})}{\mathcal{L}(\mathcal{D}|H_0)} \right], \quad (1)$$

where the data distribution under the alternative hypothesis is parametrized by a family of models  $\mathcal{F} = \{f_{\theta}, \theta \in \Theta\}$ , with unknown parameters  $\theta$  to estimate from the data

$$n(\mathbf{x}|H_{\theta}) = n(\mathbf{x}|H_0)e^{f_{\theta}(\mathbf{x})}. \quad (2)$$

For extended likelihoods [36], the maximum likelihood problem becomes equivalent to minimizing the custom loss function [37]

$$L_{\text{NP}}[f_{\theta}] = \sum_{\mathbf{x} \in \mathcal{R}} w_{\mathcal{R}} (e^{f_{\theta}(\mathbf{x})} - 1) - \sum_{\mathbf{x} \in \mathcal{D}} f_{\theta}(\mathbf{x}), \quad (3)$$

with  $w_{\mathcal{R}}$  balancing for the different samples size. The test statistic is then readily extracted from the loss function as

$$t_{\text{NP}}[f_{\theta}] = -2 \cdot L_{\text{NP}}[f_{\theta}]. \quad (4)$$

Recent studies comparing the NP test with alternative two-sample tests have found the NP test more sensitive and universally more robust to various source of anomalies in the data, especially in challenging detection regimes [33], [38], [39].

a) *Related work:* Statistical anomaly detection addresses the problem of identifying significant distributional deviations from a reference probabilistic model describing the data-generating process under nominal conditions. When the reference model must be inferred from data rather than specified a priori, the problem is naturally formulated as a *two-sample test*. An extensive body of literature on traditional statistical methods exists to address univariate setups (the most known tests are Kolmogorov-Smirnov, Anderson-Darling, Cramer-von-Mises,  $\chi^2$ ), some of which can be extended to few dimensions under specific assumptions [40], [41]. Kernel-based two-sample tests relying on the maximum mean discrepancy metric [42] provide a powerful solution to high-dimensional problems, despite the computational cost on large samples [43], [44]. More recent strategies leverage deep neural networks to learn discriminative structures: a binary classifier is trained between samples, and its performance metrics or score distributions are used as test statistics [28], [45], [46]. While effective with abundant anomalies, these approaches loose performance in regimes of low anomaly fraction.

### C. Desiderata of detection methods in challenging regimes

The power of the NP test depends on the design and optimization of the family of functions  $\mathcal{F}$  parametrizing the density-ratio. In the challenging regimes of low-anomaly fraction and separability, we argue that locality, sparsity and competition are a powerful set of inductive biases for sensitive and interpretable detection based on the NP test.

<sup>1</sup>These properties can only be assessed in presence of ground truth knowledge about the anomaly. The anomaly fraction can be quantified as the ratio between the number of anomalous points and the total number of points in the dataset. The anomaly separability can be quantified as the classification accuracy of a supervised binary classifier between anomalous and normal data points.

a) *The case for locality*: In structured data representations, it is reasonable to expect anomalies to emerge as local patterns. The vast majority of current state-of-the-art deep learning models build upon computational units based non-local activations such as ReLU [47]. Despite their numerous benefits, non-local activations require several degrees of freedom to build localized activations, making it hard to disentangle the role of different parameters in the model’s response to a specific input data point [22]. Conversely, local activations are naturally endowed with this feature [48], [49]. An illustration of this phenomenon is presented in Figure 2, where a radial-based activation (e.g. Gaussian activation) is compared to linear activation (e.g. ReLU). Radial, distance-based activations enable a geometric interpretation of the model response, directly associating a Gaussian’s location to the activated regions of the data space.

b) *The case for competition and self-organization*: The lack of information about the location of the anomaly requires learning dynamics that can efficiently explore the feature space, and ultimately localize the anomalous region. To this end, a relevant property of a good anomaly detection model is the ability to self-organize its degrees of freedom. This can be achieved by instilling *competition* between kernels during the learning stage. Competition in biological systems induces *specialization* among different agents that result in a more efficient representation of heterogeneous data [50]. Prior studies on likelihood inference with Radial Basis Function Networks (RBFNs) [51] demonstrated that introducing competition among units, most effectively through SoftMax-induced soft competition, enhances model performance.

c) *The case for sparsity*: Lastly, anomaly detection aims to single out rare patterns in the data while overlooking variability that is typical of the system and manifests as nuisance. Imposing *sparsity* in the model activation enforces an additional competing mechanism, that acts among the training data points craving for the model’s attention. Sparsity constraints in machine learning and artificial intelligence play a crucial role in enhancing model interpretability, efficiency, and generalization [52]. By enforcing that only a small subset of features, neurons, or basis functions are active at any given time, sparsity mimics the energy-efficient way biological neural networks operate in the context of sensory processing, where neurons in the brain exhibit localized and selective responses to stimuli, reducing redundancy and enhancing discriminative power [53].

#### D. Architecture design

To operationalize these desiderata in the NP test we introduce SparKer, a self-organizing-ensemble of Gaussian kernels. We consider  $d$ -dimensional Gaussian kernel acting on Euclidean space:

$$k_{\mu}^{\sigma}(\mathbf{x}) = \exp \left[ -\frac{1}{2}(\mathbf{x} - \mu)^T \Sigma^{-1}(\mathbf{x} - \mu) \right] \quad (5)$$

with location  $\mu = (\mu^1, \dots, \mu^d) \in \mathbb{R}^d$  and uniform diagonal covariance matrix  $\Sigma = \sigma^2 \mathbb{I}^{d \times d} \in \mathbb{R}^{d \times d}$ .

Inspired by Radial Basis Function Networks (RBFNs) [54-57], we build a sparse ensemble of  $M$  Gaussian kernels, with an additional competitive activation promoting the self-organization of the kernels. By denoting the vector of the  $M$  kernels embeddings as  $\mathbf{k}_{\mu}^{\sigma}(\mathbf{x}) = (k_{\mu_1}^{\sigma}(\mathbf{x}), \dots, k_{\mu_M}^{\sigma}(\mathbf{x})) \in \mathbb{R}^M$  and the vector of the kernels’ amplitudes as  $\mathbf{a} = (a_1, \dots, a_M) \in \mathbb{R}^M$ , we define SPARKER, as

$$f_M^{\sigma}(\mathbf{x}) = \mathbf{a}^T [\mathbf{p}[\mathbf{k}_{\mu}^{\sigma}(\mathbf{x})] \odot \mathbf{k}_{\mu}^{\sigma}(\mathbf{x})], \quad (6)$$

where  $\odot$  denotes the Hadamard product between the vectors. The functional  $\mathbf{p} : \mathbb{R}^M \rightarrow \mathbb{R}^M$  is an activation function

$$p^i[\mathbf{k}_{\mu}^{\sigma}(\mathbf{x})] = \frac{k_{\mu_i}^{\sigma}(\mathbf{x})}{\sum_j k_{\mu_j}^{\sigma}(\mathbf{x})}, \quad (7)$$

that is formally analogous to applying a SoftMax to the negative of the data-to-locations squared Euclidean distance, with temperature  $2\sigma^2$ . The vectors of kernels’ locations  $\mu$  and amplitudes  $\mathbf{a}$  are the parameters to estimate, while the kernels’ width  $\sigma$  is treated as a hyperparameter and is annealed during training, allowing to scan over multiple assumptions of locality. Sparsity is hard coded in the model by keeping the number of kernels  $M$  much smaller than the training sample size, and further encouraged by the SoftMax activation function. Details on model initialization and hyperparameters selection are available in the Supporting Information of this paper.

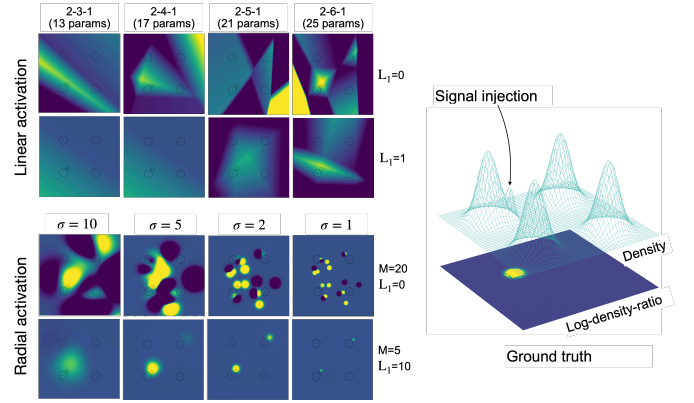


**Fig. 2: Local layers enable geometric interpretation of activation patterns.** Examples of 2D log-density ratio approximated by a 1-layer model with ReLU activation (top left grid) and mixture of Gaussian kernels (bottom left grid) subject to different sparsity constraints. The local activation characterizing Gaussian kernels enables efficient selection of convex regions, whereas linear activation requires the interplay of multiple parameters, undermining interpretability. We report on the right side the ground truth of the log-density ratio function targeted by the model, as well as the density of the sample with injected anomalies.

**Algorithm 1** SPARKER. algorithm

---

```

1: Calibration Experiments:
2: Build a set of anomaly-free bootstrapped datasets:  $S_0 = \{\{\mathbf{x}_i\}_{i=0}^{N_{\mathcal{D}}} \mid \mathbf{x} \sim p(\mathbf{x}|\mathbf{H}_0)\}$ 
3: for all  $\mathcal{D}_0 \in S_0$  do
4:   Train  $f_M^\sigma$  with linear  $\sigma$ -annealing on  $\mathcal{R}$  and  $\mathcal{D}_0$  to minimize Eq. 3
5:   Store  $m$  intermediate model configurations:  $(f_M^{\sigma_1}, \dots, f_M^{\sigma_m})$ 
6: end for
7: for all  $\mathcal{D}_0 \in S_0$  do
8:   for all  $\sigma \in [\sigma_1, \dots, \sigma_m]$  do
9:     Extract test  $t_{\text{NP}}[f_M^\sigma](\mathcal{D}_0)$  as in Eq. 4
10:    Compute  $p$ -value:  $p_\sigma(\mathcal{D}_0) = 1 - \text{EDF}[t_{\text{NP}}[f_M^\sigma](\mathcal{D}_0)]$ 
11:   end for
12:   Compute the combined test:  $p(\mathcal{D}_0) = -\frac{1}{2} \min_{\sigma} [\log p_\sigma(\mathcal{D}_0)] - \frac{1}{2m} \sum_{\sigma} \log p_\sigma(\mathcal{D}_0)$ 
13: end for
14: Collect all calibration  $p$ -values:  $P_0 = \{p(\mathcal{D}_0) \mid \mathcal{D}_0 \in S_0\}$ 

15: Anomaly Detection:
16: Consider the dataset of interest  $\mathcal{D}$ 
17: Train  $f_M^\sigma$  with linear  $\sigma$ -annealing on  $\mathcal{R}$  and  $\mathcal{D}$  to minimize Eq. 3
18: Store  $m$  intermediate model configurations:  $(f_M^{\sigma_1}, \dots, f_M^{\sigma_m})$ 
19: for all  $\sigma \in [\sigma_1, \dots, \sigma_m]$  do
20:   Extract test  $t_{\text{NP}}[f_M^\sigma](\mathcal{D})$  as in Eq. 4
21:   Compute  $p$ -value:  $p_\sigma(\mathcal{D}) = 1 - \text{EDF}[t_{\text{NP}}[f_M^\sigma](\mathcal{D})]$ 
22: end for
23: Compute the combined test:  $p(\mathcal{D}) = -\frac{1}{2} \min_{\sigma} [\log p_\sigma(\mathcal{D})] - \frac{1}{2m} \sum_{\sigma} \log p_\sigma(\mathcal{D})$ 
24: Compute global  $p$ -value:  $P = \frac{\sum_{\mathcal{D}_0 \in S_0} \mathbb{I}[p(\mathcal{D}_0) > p(\mathcal{D})]}{|S_0|}$ 

```

---

*E. Testing pipeline*

In an initial ‘‘calibration’’ phase, the algorithm is run multiple times with bootstrapped data that follows the anomaly-free distribution. For each trial, we collect the outcome of the test and use the resulting empirical distribution to calibrate the  $p$ -value, e.g. to assess the rate of false positives. This phase is blind to the anomaly nature and is kept as generic as possible. The hyper-parameters of the model can be tuned at this stage to improve the shape of the test statistic distribution (details on this aspect of model design can be found in the Supporting Information). The second phase is the actual anomaly detection, in which we run SPARKER. on the data of interest and we compute an observed  $p$ -value exploiting the calibration distribution obtained in the previous stage. The main steps of the algorithm are summarized in Algorithm 1.

## III. THEORETICAL ANALYSIS OF SPARKER

In this section, we analyze the properties and training dynamics of the SPARKER. model, providing theoretical insights and simple experiments that clarify the mechanisms that drive its detection performance. Proofs and additional details are reported in the Supporting Information.

*A. An energy-based interpretation of SparKer*

The update rules for a generic trainable parameter of the SPARKER. model follows gradient descent on the NP loss

$$\theta_{t+1} - \theta_t = \Delta\theta_t \propto - \left. \frac{\partial_{\theta} L_{\text{NP}}[f_{\theta}]}{\partial \theta} \right|_{\theta=\theta_t}, \quad (8)$$

where  $L_{\text{NP}}$  is the NP objective, whose gradient with respect to a generic parameter  $\theta$  reads as

$$\partial_{\theta} L_{\text{NP}}[f_{\theta}] = w_{\mathcal{R}} \sum_{\mathbf{x} \in \mathcal{R}} e^{f_{\theta}(\mathbf{x})} \partial_{\theta} f_{\theta}(\mathbf{x}) - \sum_{\mathbf{x} \in \mathcal{D}} \partial_{\theta} f_{\theta}(\mathbf{x}). \quad (9)$$

The action of the two training sets  $\mathcal{D}$  and  $\mathcal{R}$  on the gradient of the loss is asymmetric. To better understand how the asymmetry impacts the gradient dynamics, we study the continuum limit of Eq. 20<sup>2</sup>:

$$\begin{aligned} \partial_{\theta} L_{\text{NP}}[f_{\theta}] &\rightarrow \int d\mathbf{x} [n(\mathbf{x}|\text{H}_0)e^{f_{\theta}(\mathbf{x})} - n(\mathbf{x}|\mathcal{D})] \partial_{\theta} f(\mathbf{x}) \\ &= \int d\mathbf{x} [n(\mathbf{x}|\text{H}_{\theta}) - n(\mathbf{x}|\mathcal{D})] \partial_{\theta} f_{\theta}(\mathbf{x}) \\ &\approx \sum_{\mathbf{x} \in \hat{\mathcal{D}}} \partial_{\theta} f_{\theta}(\mathbf{x}) - \sum_{\mathbf{x} \in \mathcal{D}} \partial_{\theta} f_{\theta}(\mathbf{x}). \end{aligned} \quad (10)$$

Due to the parametrization in Eq. 2, summing the gradients of the model over the dataset  $\mathcal{R}$  weighted by the exponential factor  $e^{f_{\theta}(\mathbf{x})}$  is equivalent, in the limit of large statistics, to summing the gradients of the model over a dataset  $\hat{\mathcal{D}}$  generated according to the approximate model of the data,  $\text{H}_{\theta}$ , learned during training. The dynamics finds a point of equilibrium when the force resulting from the system of data points  $\hat{\mathcal{D}}$  equals the force resulting from the real data  $\mathcal{D}$ . In other words, the optimization goal is to find a function  $f_{\theta}$  which *generates* a representation of the dataset of interest  $\mathcal{D}$  that matches the energy of the system (e.g. has the same distribution). This binary regression dynamic thus implicitly hides an *energy-based model* [58], [59] describing a system of interacting particles. The kernels' locations represent hidden units while the datasets  $\mathcal{D}$  and  $\mathcal{R}$  are respectively positive and negative visible units, defining an environment to which the hidden units have to adapt (see Figure 3). Regions with an asymmetry between the two samples density drive the dynamics until the model  $f_{\theta}$  learns to generate a data density model  $n(\mathbf{x}|\text{H}_{\theta})$  locally equivalent to the data model  $n(\mathbf{x}|\mathcal{D})$ .

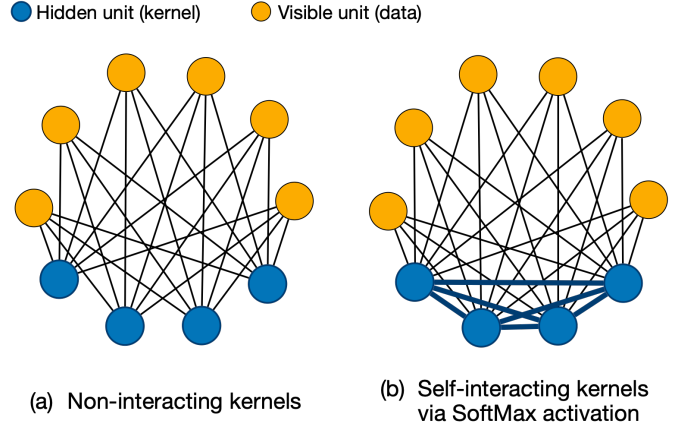


**Fig. 3: Interpreting SPARKER as a system of interacting particles.** The training data (i.e. the visible units) in orange represent the system environment while the kernels (i.e. hidden units) are latent variables of the system, capturing higher order correlations in the data patterns. In the absence of the SoftMax activation (left graphics), the hidden units interact with the environment but are not aware of each others. SoftMax activation introduces an interaction term between kernels that promotes a joint optimization and units specialization (right graphics).

### B. Learning dynamics as a system of particles

Eq. 10 shows that real and “generated” data contribute to the kernels’ dynamics proportionally to the gradient of the model evaluated at that point. For the amplitude of the  $i^{\text{th}}$  kernel, the contribution of each data point  $\mathbf{x}$  to the gradient of the model takes the form of a scalar field locally active around the kernel’s means and vanishing far from it:

$$\partial_{a_i} f(\mathbf{x}) = p_i [\mathbf{k}_{\mu}^{\sigma}](\mathbf{x}) \cdot k_{\mu_i}^{\sigma}(\mathbf{x}). \quad (11)$$

On the other hand, the gradient of the location of the kernel  $\mu_i$  has the form of a radial vector field

$$\partial_{\mu_i} f(\mathbf{x}) = A_i(\mathbf{x}) \cdot \mathbf{r}_i, \quad (12)$$

where  $\mathbf{r}_i = \mathbf{x} - \mu_i$  is the displacement vector between the kernel location and the data point in Euclidean space, and  $A_i(\mathbf{x}) = \frac{1}{\sigma^2} \cdot [2a_i k_{\mu_i}^{\sigma}(\mathbf{x}) - f_M^{\sigma}(\mathbf{x})] \cdot p_i [\mathbf{k}_{\mu}^{\sigma}](\mathbf{x})$  is the magnitude.

The radial nature of the gradient in Eq. 12 let us identify “push-pull” dynamics between pairs of kernels and training points that, in turn, induce the kernels to self-organize. We formalize this behavior in the following lemma:

**Lemma 1** (Push-pull dynamic of kernels’ locations). *The dynamics of the  $i^{\text{th}}$  kernel location  $\mu_i$  is the result of radial forces arising from the training points. Let  $y$  be the class label associated with each data point ( $y = 0$  for  $\mathbf{x} \in \mathcal{R}$  and  $y = 1$  for  $\mathbf{x} \in \mathcal{D}$ ), and let  $m_i(\mathbf{x}) = 2a_i k_i(\mathbf{x}) - f(\mathbf{x})$  be the  $i^{\text{th}}$  kernel “mass charge” in  $\mathbf{x}$ . Each interaction is:*

$$\begin{aligned} \text{“radially attractive”} &\quad \text{if } m(\mathbf{x}) \cdot (2y - 1) > 0 \\ \text{“radially repulsive”} &\quad \text{if } m(\mathbf{x}) \cdot (2y - 1) < 0 \end{aligned}$$

<sup>2</sup>Assuming the integral is finite, the approximation in Eq. 10 follows from the strong law of large numbers

a) *A scale-dependent, local dynamic*: Notably, the gradients in Eq. 12 and 11 are *local* and *scale dependent*, and only data points that are in the neighborhood of a kernel have a leading role in them. We formalize this phenomenon by defining an active region for a kernel’s dynamics that has radial geometry:

**Definition 1** (Kernel radial  $\alpha$ -level). *Let  $k : \mathbb{R}_+ \rightarrow \mathbb{R}_+$  be a continuous, radial kernel profile that is nonincreasing in  $r \geq 0$  (i.e.  $k(r_1) \geq k(r_2)$  for  $r_1 \leq r_2$ ). For a given level  $\alpha \in (0, k(0))$  define the radial  $\alpha$ -level  $r_\alpha$  as the radius such that  $k(r) < \alpha \quad \forall r > r_\alpha$ , or equivalently  $r_\alpha = \sup\{r \geq 0 : k(r) \geq \alpha\}$ .*

The radial  $\alpha$ -level delineates each kernel’s *sphere of influence*, the region where data points meaningfully influence the location  $\mu$  and amplitude  $a$  dynamics:

**Lemma 2** (Kernel’s Sphere of Influence). *For each kernel  $i$  that makes up the SPARKER. model, there exists a value  $\alpha \in (0, 1)$  such that the associated ball  $S_i^\sigma(\alpha) = \{\mathbf{x} \in \mathbb{R}^d : \|\mathbf{x} - \mu_i\| \leq q_i^\sigma(\alpha)\}$  contains all the training points that contribute at least  $\epsilon_\alpha$  to the kernel’s dynamics, i.e., points outside this ball have no more than  $\epsilon_\alpha$  effect on the kernel’s dynamics. We name this ball the kernel’s “Sphere of Influence”:*

$$\exists \epsilon_\alpha > 0 \quad \text{s.t.} \quad |\partial_{\theta_i} f(\mathbf{x})| < \epsilon_\alpha, \quad \forall \mathbf{x} \notin S_i^\sigma(\alpha)$$

*If  $\alpha \ll 1$  then  $\epsilon_\alpha \ll 1$  as well. In other words, dynamics are local on a scale that is determined by the kernels’ width,  $\sigma$ .*

### C. Explore and exploit via scale annealing

An AD algorithm exhibits strong detection power when it assigns high scores to anomalous regions while maintaining low scores across the rest of the data distribution. This requires that at least one kernel of SparKer’s identifies the anomalous region, and that its resolution (i.e., the kernel width  $\sigma$ ) is sufficiently fine to distinguish it from the background. Hence, discovering anomalous regions requires the kernels to simultaneously explore the data space, and resolve the anomaly. However, due to the local nature of the Sphere of Influence, exploration is only possible with broad kernels, while resolution requires narrow ones. We address this challenge using deterministic annealing over  $\sigma$  [60], analogous to lowering the temperature of the system of particles. At high temperatures (large  $\sigma$ ), kernels behave like diffusive particles that explore the space broadly, avoiding poor local minima. As the temperature decreases (smaller  $\sigma$ ), their interactions become more localized, allowing the ensemble to condense and specialize around regions of anomalous density.

**Lemma 3** (Scale annealing leads to localization). *Monotonically annealing the kernel scale  $\sigma$  shrinks the size of the Sphere of Influence:*

$$\sigma_t < \sigma_{t-1} \implies \text{Vol } S_i^{\sigma_t}(\alpha) < \text{Vol } S_i^{\sigma_{t-1}}(\alpha),$$

*resulting in a decrease in the number of data points that influence the dynamics of each kernel  $i$ .*

Gradually annealing  $\sigma$  leads to regimes where, eventually, only one data point remains in the sphere of influence. In this setting, SPARKER. provably converges to that point within the Sphere of Influence:

**Theorem 1** (Local convergence). *If  $S_i^{\sigma_t}$  contains only one data point  $\mathbf{x}^*$ , then  $\mu_i$  converges radially towards  $\mathbf{x}^*$ , getting  $\epsilon$ -close to  $\mathbf{x}^*$  in  $O(\log 1/\epsilon)$  further steps.*

Empirically, we observe that the combination of scale-annealing and training objective leads the kernels to statistically imbalanced (e.g. anomalous) regions of the data space. Figure 4 illustrates the dynamics of kernels’ locations for a two-dimensional toy problem, where a 4-kernel SPARKER. model is asked to fit three anomalous regions, highlighted in yellow.

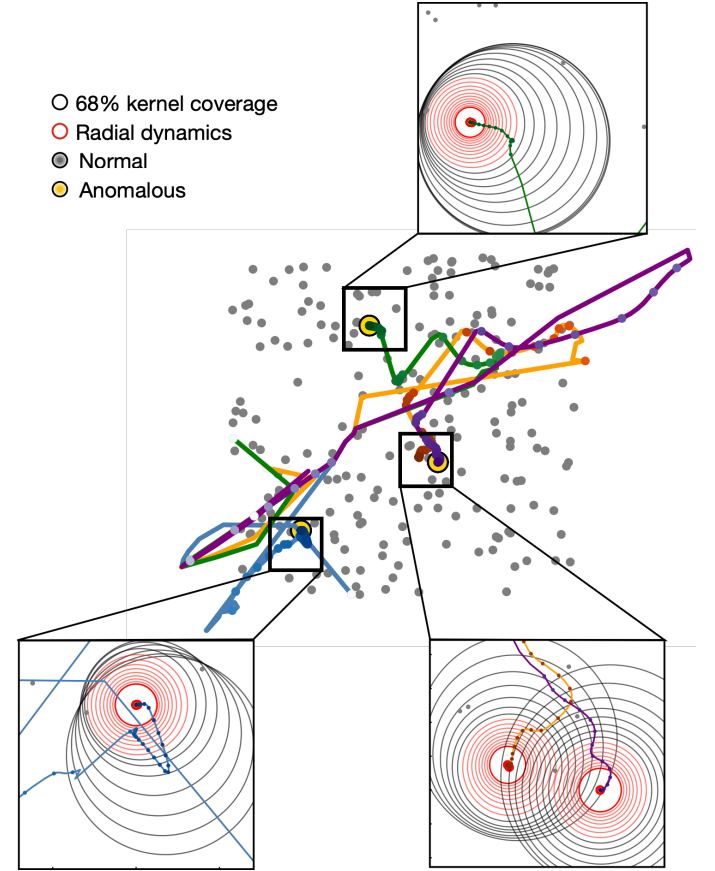


**Fig. 4: Attraction and repulsion govern kernels’ learning dynamics.** Example of kernels’ trajectories over training time in a 2-dimensional setting where normal data are uniformly distributed in a square (gray points). Three sources of anomalies, highlighted in yellow, are injected in the data. We run a 4-kernels SPARKER. model and examine the kernels’ self-organization dynamics represented by the colored lines. Two stages can be identified in the dynamics: a first stage in which the kernels are broad and pushed to explore the space, and a second stage in which progressively narrow kernels are radially attracted towards the anomalous regions (see zoomed out panels).

The four sequences of colored dots represent the four kernels’ trajectories during training. Early in the learning process, broad kernels encourage exploration by spreading across the data space. As training progresses, the dynamics shift toward refinement, with narrower kernels specializing on distinct regions and capturing fine-grained structure. After some time  $t$ , the kernels enter a phase of radial convergence (highlighted in red in the figure zoom out) towards the only active point left in their Sphere of Influence.

To further demonstrate the detection power enabled by scale annealing, we perform a 1-dimensional toy experiment. Within a teacher–student framework [61], the data are assumed to be generated by an underlying teacher model, while the student model, here represented by SparKer, attempts to infer its structure through optimization.

The data distribution in normal conditions is the mixture of two Gaussian models with unitary scale and locations  $c_{\pm} = \pm 3$ , symmetric with respect to the origin. The signal consists of one anomalous point located at  $x^* = -10$ . We consider the limit of infinite statistics, e.g.  $N \gg 1$ , where statistical fluctuations are negligible, and we train a 1-kernel model either without annealing, selecting few different choices of the kernel’s width ( $\sigma = 5, 1, 0.5, 0.05$ ), or with linear annealing. For a fair comparison, all configurations start from the same initialization. Figure 5 shows the evolution of the kernel’s distance to the anomaly as a function of training time for the various width choices. For a finite number of epochs, an accurate localization of the anomaly only occurs for an appropriate choice of the scale (e.g.  $\sigma = 1$ ) or using annealing. Kernels that are too broad fail at localizing the anomaly, while ones that are too narrow evolve too slowly due to their gradient vanishing far from the anomaly. Annealing makes it possible to both locate the anomaly and arbitrarily increase the detection resolution by gradually reducing the width.

#### D. Competition between kernels, interaction and self-organization

While annealing provides an elegant solution to efficient exploration, it alone does not take advantage of the collective properties of the ensemble. The specialization of the kernels is further enhanced by competitive nature of the SoftMax activation. SoftMax promotes competition because its output must sum to one. Thus, SparKer’s gradients with respect to a generic kernel’s location  $\mu_i$  are altered by the presence of nearby kernels. Nearby kernels with the same sign that are simultaneously active in a region of the input space compete with each other to represent it. The kernel with the largest activation repels the others and wins the competition. These dynamics cause a spontaneous self-organization of the kernels in the space, which privileges low entropy configurations.

This is a desirable property of the model as it promotes specialization of the kernels beyond exploration, making the model more interpretable. At the same time, it leads to higher chance of detecting multiple signals, as well as avoiding local minima arising due to statistical fluctuations.

To demonstrate the impact of the Softmax activation on the detection abilities of the model, we study a one-dimensional toy model where the data distribution in normal conditions is the mixture of two Gaussian models defined in Section III-C. The signal consists of two anomalous points located at different distances from the origin ( $x_1^* = -5$ ,  $x_2^* = -10$ ), so that their anomaly strength is different. We train a 2-kernel model with and without SoftMax activation and report in Figure 6 the evolution of the locations of the two kernels during training. In absence of SoftMax, both kernels converge to the location of the leading anomaly, whereas in its presence, the repulsion between the kernels forbids them to collapse on the same anomaly, thus enabling the discovery of the secondary anomaly.

The other crucial benefit of the SoftMax activation is the ability to escape local minima caused by statistical fluctuations. Statistical fluctuations can give rise to over- and under- density of similar local significance than a real anomaly. SoftMax discourages the kernels to collapse on a single local solution, promoting exploration, eventually increasing the chance of escaping local traps. To illustrate this phenomenon, we consider a second experiment on the one-dimensional toy model defined by the mixture of two Gaussian models. A signal is generated according to an additional Gaussian distribution with location  $x^* = -5$  and scale 0.1. To study the impact of statistical fluctuations, we consider a training set with limited sample size. We trained two 7-kernel SPARKER. models differing only for the presence of the SoftMax activation. Figure 7 shows the evolution of the kernels during training for the models with SoftMax activation (right panel) and without (left panel). In the absence of SoftMax, the kernels tend to collapse into fewer locations dominated by statistical fluctuations, missing the anomaly located at  $-5$ . Conversely, with SoftMax, the kernels explore the space better and eventually identify the anomaly.

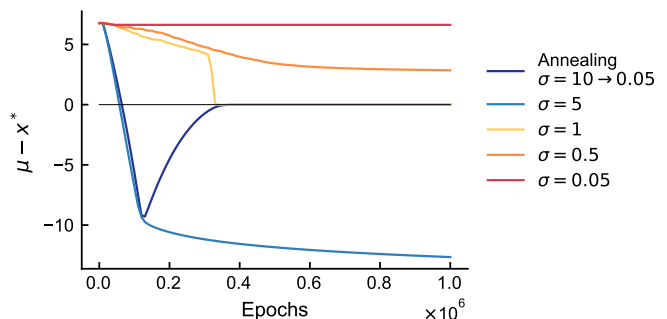


**Fig. 5: Scale annealing overcomes the vanishing gradient leading to convergence.** Kernel distance from anomalous point as a function of training time using linear annealing (blue line) or a fixed value of the kernel width (other colors). Kernels that are too wide or too narrow either do not localize the signal or do not converge in a reasonable amount of time. With  $\sigma = 1$ , the model localizes the signal. With annealing, the model localizes the signal with progressively higher resolution.

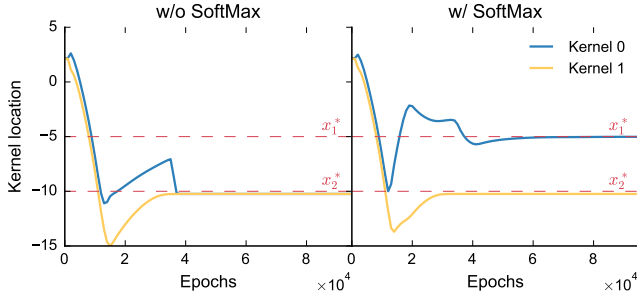


**Fig. 6: The SoftMax activation helps exploration.** Evolution over training of the location of the kernels in the 2-kernel SPARKER. model with (right panel) and without (left panel) SoftMax. The SoftMax activation makes the kernels repel each other, allowing the model to discover both the dominant anomaly at  $x = -10$  and the secondary anomaly at  $-5$ . In its absence, the model only discovers the dominant anomaly.

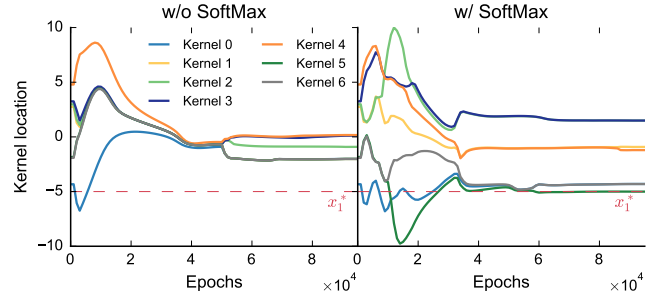


**Fig. 7: The SoftMax activation helps escaping local traps.** Evolution over training of the location of the kernels in a 7-kernel SPARKER. model with (right panel) and without (left panel) SoftMax activation. SoftMax induces a repulsion between kernels that allows the model to discover the real anomaly at  $x = -5$ , despite statistical fluctuations.

The theoretical analysis and controlled experiments presented in this Section highlight the strong detection performance of SPARKER. in regimes of low-anomaly separability and fraction. Additional experiments on simple one- and two-dimensional problems, reported in the Supporting Information, further assess the effect of modeling choices on detection power. Experiments over multiple data realizations and initial conditions show that (1) in regimes of signal scarcity and low separability, the NP loss systematically leads to higher performances than alternative binary classification losses, like Binary cross Entropy or Mean Square Error; (2) including SoftMax systematically promotes uniform kernel distribution over the space, enhancing sensitivity. Moreover, we assess the robustness of the test across signal benchmarks spanning different AD regimes. We find that the performance of SPARKER. is fairly robust even in scenarios where sparsity and locality cease to be optimal assumptions.

#### IV. APPLICATIONS

We apply SPARKER. to a broad set of AD benchmarks encompassing scientific discovery, open-world novelty detection, intrusion detection, and validation of generative AI models. Despite differences in application domain, data modality, and feature-space dimensionality, these problems exhibit similar characteristics—in particular, anomalies have low separability—as illustrated in Fig. 1(a).

##### A. Baselines

To put the performance of SPARKER. in its proper context, we compare the results of our experiments with two baseline AD methods. Both methods rely on kernel methods. They differ in the assumptions and design choices they make. In both cases, we ensemble over multiple kernel bandwidths, initialize their locations randomly from data and do not train the latter. The baselines we select are described in the following.

*a) Kernel-based Neyman-Pearson test (Falcon).*: We implement the NP test with kernel logistic regression as introduced in [35]. The implementation exploits the Falcon library [62], which combines fast iterative solvers with a Nyström approximation of the kernel matrix projected onto a low-rank subspace defined by a small set of locations. In this setting, the model is effectively a linear combination of Gaussian kernels whose centers are the selected locations, chosen randomly from the data and kept constant during training. For a fair comparison, we ensemble over multiple kernel bandwidths and combine the tests using the minimum  $p$ -value, following the procedure from [17].

*b) Nyström Maximum Mean Discrepancy (Nyström-MMD).*: Maximum Mean Discrepancy (MMD) [42], [63] is a kernel-based metric for comparing distributions that avoids density estimation and has been widely used in generative model evaluation and domain adaptation. Variants of MMD enhance interpretability and detection power by optimizing witness functions [64–66] or exploiting multiple scales [67], [68]. We implement the recently-proposed Nyström-MMD [43], which approximates the kernel matrix via low-rank Nyström projections, reducing complexity while preserving minimax-optimal power guarantees, thus enabling scalable two-sample testing in high dimensions. With this approximation, we compute a robust version of MMD called MMDfuse [67], where MMD tests with different values of the kernel width are aggregated via the log-sum-exp rule.

##### B. Scientific discovery

Novelty discovery in scientific domains is often times characterized by extremely rare signals of unknown location and nature, making the desiderata we operationalize in SPARKER. particularly suitable. We can construct a reference sample either via simulation of a theoretical model or by means of well-understood data. We claim discovery at level  $\alpha$  when newly-collected

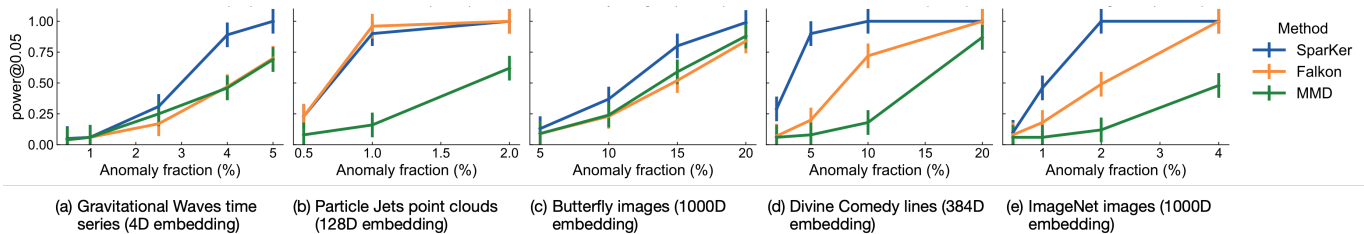


**Fig. 8: Sensitivity study: detection power as a function of anomaly fraction.** We report the performance of SPARKER. in terms of detection power at 5% false positive rate as a function of the anomaly fraction. Error bars represent the Clopper-Pearson 68% confidence intervals. We consider various applications, differing in raw-data modality, anomaly fraction and the dimension of the feature space in which we embed the data: we embed gravitational-waves time series into a 4-dimensional representation (panel (a)), point clouds representing particle jets in a 128-dimensional space (panel (b)); butterfly images and ImageNet data in a 1000-dimensional space (panel (c) and (e)), and lines from Dante’s Divine Comedy in a 384-dimensional-space (panel (d)). We report additional details about the experiments in the Supporting Information.

data deviates from the reference with a  $p$ -value less than  $\alpha$ . We present three examples of signal-agnostic novelty detection for scientific discovery, spanning the fields of astrophysics, particle physics and genomics. We encode data from the different modalities, namely time series of gravitational waves in astrophysics, point clouds from particle jets, and butterfly images from genomics, in rich latent representations and compare to a nominal dataset using SparKer. For the gravitational waves and particle jets, the nominal sample consists of synthetic data coming from well controlled simulations of a theoretical model. For the application to genomics, the ground truth comprise experimental data labeled as nominal by experts in the field. We defer implementation details and the descriptions of datasets to the Supporting Information. Panels (a), (b) and (c) in Figure 8 report the detection performance of SparKer, compared to the Falkon and MMD baselines for the three use cases. We report the test power at a 5% false positive rate as a function of the fraction of anomalous signal injected in the sample. SPARKER. consistently performs similarly to or outperforms the baselines.

### C. Open-world novelty detection

Out-of-domain (OOD) detection is a key task for assessing the robustness and safety of machine learning (ML) systems trained under the *closed-world* assumption [14]. OOD inputs—originating from the *open world*—differ from the training distribution, leading to unreliable model predictions. Detecting such inputs is therefore essential for trustworthy ML deployments [69]. In computer vision, numerous methods have been benchmarked on standard datasets [70], relying on measures of the extent to which data lie out of distribution (“outness”) based either on classification, density or distance. However, a recent study [25] shows that many of these strategies are misaligned with the OOD detection objective: rather than determining whether a sample originates from the training distribution, they assess its feature proximity or prediction uncertainty, proxies that do not capture distributional novelty reliably. To illustrate this, we test SPARKER. on the 1000-dimensional latent space of a ResNet50 classifier trained on ImageNet-1000 [71], injecting “Striped” samples from the Textures dataset [72] as OOD anomalies. The network classifies “Striped” data with high confidence, highlighting the exposure of logit-based OOD detection to failure modes [25]. We report SparKer’s detection power as a function of anomaly fraction in panel (e) of Figure 8. With a calibration set comprising 300 samples and an anomaly fraction as low as 2%, we find an upper limit on the empirical  $p$ -value of 0.003, indicating a disagreement between the dataset containing the Striped intrusions and the closed world data at the level of  $2.7\sigma$  or higher. Moreover, turning the likelihood-ratio model SPARKER. estimated into an anomaly score, we find, at 95% true positive rate (FPR@%95), that SPARKER. exhibits a false positive rate of 2.5%, in sharp contrast to standard logit-based methods that exhibit a FPR@%95 as high as 66% [25].

### D. Intrusion detection

We prompted Meta-Llama-3-70B-Instruct [73] to randomly generate lines from Dante’s Divine Comedy and embedded these into 384-dimensional-representations using multilingual Sentence-BERT [74]. We tested samples comprising 1000 lines. To simulate a problem of intrusion detection, we injected 2 to 20% AI generated lines in the dataset and tested SparKer’s power of detection. Similar to the scientific discovery and open-world settings, we compared the performance of SPARKER. performance to those of Falkon and MMD. SPARKER. keeps almost full power for anomaly injection as low as 5%, indicating that its power is five times as large as those of Falkon and MMD. This enables the detection of subtle anomalous patterns that could otherwise not be discovered (see panel (d) of Figure 8).

### E. Validation of Generative AI

Another relevant application of SPARKER. is the validation of generative models. AI techniques to generate artificial samples are rapidly improving, producing synthetic data that are often hard to distinguish from real ones. The ability to assess

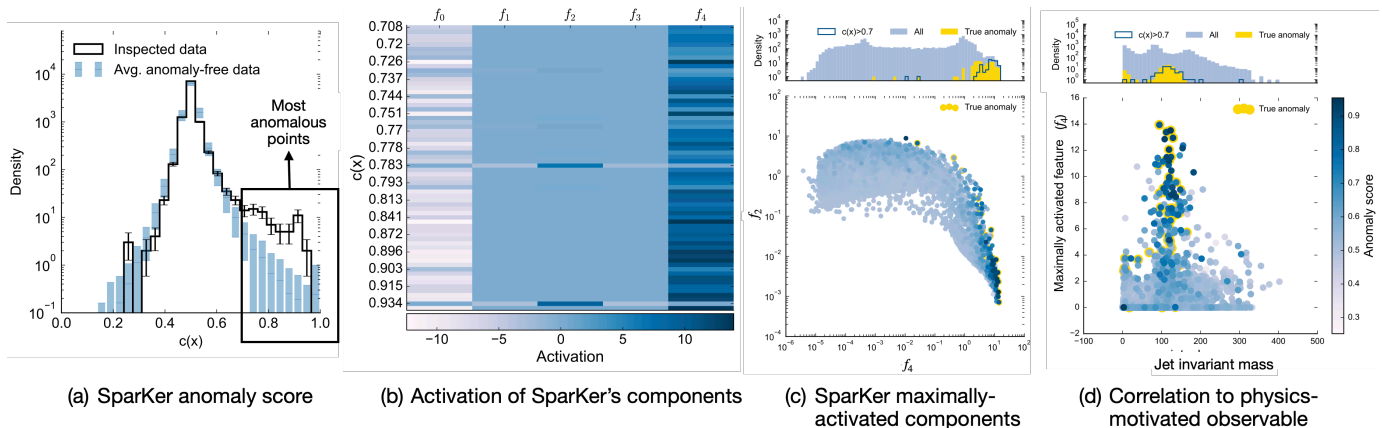


**Fig. 9: Inspecting anomalous particle jets.** (a) Distribution of the anomaly score,  $c(x)$ , over the inspected data (black histogram), compared with the average expected distribution in absence of anomalies (error bars represent the standard deviation over 100 realizations). (b) Activation pattern over SparKer’s components for the most anomalous data points. At high anomaly score,  $f_4$  and  $f_2$  are the main positively activated components. (c) Correlation of the two maximally-activated components, color coded by anomaly score. The anomalous region are pushed to the edges of the distribution. (d) Correlation of  $f_4$  with the jet’s invariant mass, a physics-motivated observable characterizing the data. Without a priori knowledge about physics, the model highlights specific values of the jet mass around 125 GeV, matching the Higgs boson mass, used as the anomalous signal in this application.

distributional shifts can highlight subtle differences between real and artificial generation processes, and identify deficiencies in the representations of concepts representations. Together, these capabilities can help the process of refining generative AI and the development of more reliable tools.

We compared the original CIFAR-10 dataset [75] with the CIFAR-5m dataset introduced in [76]. This dataset was artificially generated by sampling the DDPM unconditional generative model developed in [77] to imitate CIFAR-10. We apply SPARKER. to CIFAR-10 and CIFAR-5m samples embedded in the 1000-dimensional feature space output by a ResNet50 model pretrained on ImageNet. This representation provides a rich basis of features that is not tailored to CIFAR, making the problem harder but realistic. The CIFAR-5m generative process takes the role of reference hypothesis. We tested how well it fit the original CIFAR-10 data. Using a reference set of  $N_{\mathcal{R}} = 10^5$  and a test set of  $N_{\mathcal{D}} = 10^4$  we found an upper limit on the empirical  $p$ -value of 0.005, indicating a disagreement between the synthetic and real data distribution at the level of  $2.6\sigma$ .

## V. EXTRACTING INTELLIGIBLE KNOWLEDGE

Interpretability in AD has evolved from *post-hoc* explanations—such as feature attribution, saliency maps, and surrogate models—toward intrinsic and mechanistic approaches that embed human-understandable structure within the model itself [78]. Recent studies highlight how superposition, modularity, and representational geometry shape interpretability [79–83], motivating architectures that are transparent by design [84]. In this context, SPARKER. provides a geometric framework in which sparsity, locality, and competition yield kernel locations or features that directly map to regions of distributional deviations in the data. Below we explain how to extract geometric insights and interpretations from SparKer.

*a) Anomaly score:* The most informative output of the algorithm is the log-density ratio, namely the model  $f_M^\sigma$ , which we can transform into an *anomaly score* via the Sigmoid activation:

$$c(\mathbf{x}) = \text{Sigmoid}(f_M^\sigma(\mathbf{x})) \quad (13)$$

We can use the anomaly score to identify and select the most anomalous points in the dataset. Panels (a) of Figures 9 and 10 show two examples of anomaly-score distributions over samples containing anomalous points (black histogram). The panels also show, as a baseline for calibration, the average distributions for the anomaly-free datasets (light blue bars). The error bars represent the standard deviation among 100 replicas. Similar to standard classifiers, the anomaly score provides a degree of confidence on the anomaly label that informs us on the expected density of anomalies in a specific region of the input data domain. We can define a selection threshold on the right tail of the distribution to identify the regions with the highest detected over-density in the sample for further inspection. Similarly, selections on the left tail highlight regions with detected under-density.

*b) Geometric characterization via feature specialization:* In contrast to existing models, SPARKER. provides a geometric perspective on the anomaly score arising from the interplay of locality, sparsity, and competition. The model naturally decomposes into local components:

$$f_M^\sigma(\mathbf{x}) = \sum_{i=1}^M f_i^\sigma(\mathbf{x}). \quad (14)$$

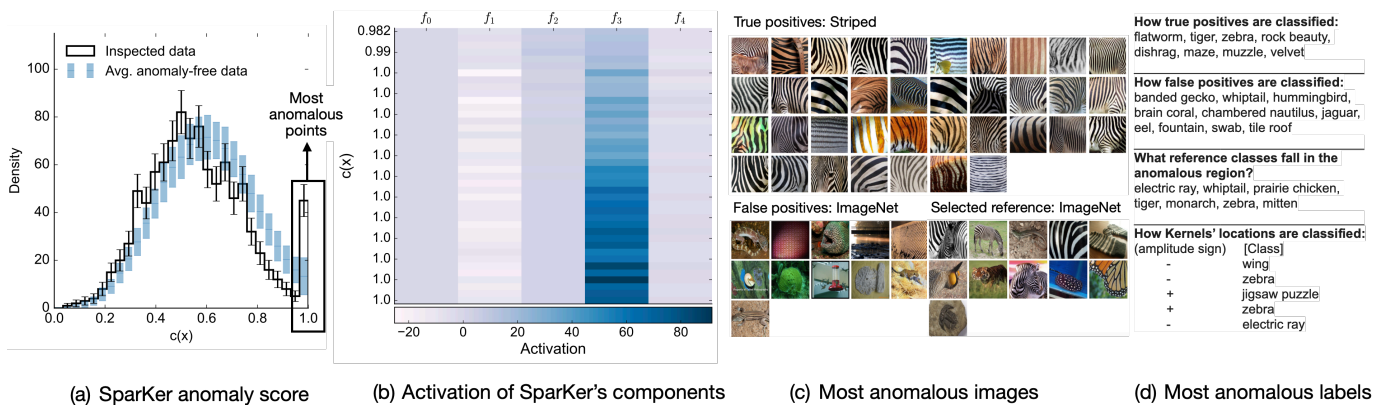


**Fig. 10: Inspecting detected open world novelties.** (a) Distribution of the anomaly score,  $c(x)$ , over the inspected data (black histogram), compared with the average expected distribution in absence of anomalies (error bars represent the standard deviation over 100 realizations). (b) Activation pattern of SparKer’s components for the most anomalous data points. The black box highlights the most active component,  $f_3$ . (c) Images associated to the most anomalous points, distinguishing between true positives coming from the “Striped” class in Textures, false positives and reference events coming from ImageNet test set. (d) Predicted labels of the most anomalous points. While localized around  $f_3$ , the anomalous points span different ImageNet classes, highlighting a non-trivial geometric structure of the anomaly.

Due to the SoftMax activation in the model’s design, different kernels specialize to different subsets of the anomalous data and activate in response to different attributes, allowing the disentanglement of role of individual kernels and their interpretation. Pairing the anomaly score with the activation pattern helps to characterize anomalies and their properties (see panel (b) in Figures 9 and 10).

In the following, we focus on three of the applications discussed in Section IV: anomalous jet discovery in particle physics, novel class discovery in open-world settings, and intrusion detection in text streams. We present complementary analyses addressing generative-model validation and butterfly-species discovery in the Supplementary Information.

*c) Interpreting novel particle jets:* Figure 9 illustrates the discovery of anomalous particle jets introduced in Section IV-B, focusing on the 1% signal injection case. Panel (b) shows that anomalous events exhibit a strong positive correlation with SPARKER component,  $f_4$ . To further characterize the signals detected, panel (d) displays the correlation between the most activated component,  $f_4$ , and a physics-motivated observable related to the jet’s invariant mass. The true anomalous points (in yellow) are strongly activated by  $f_4$  and cluster around the Higgs boson mass region (125 GeV), which corresponds to the dominant attribute of the injected signal. This demonstrates SparKer’s ability to isolate and interpret physically-meaningful structure within complex data.

*d) Extracting insights on open-world novelties:* Figure 10 summarizes the interpretability analysis of the open-world novelty detection task introduced in Section IV-C. The anomaly score distribution in panel (a) highlights the most anomalous samples, while their correlation with feature activations in panel (b) reveals that the anomalies are primarily associated with feature  $f_3$  and  $f_1$ . Applying a threshold of  $c = 0.95$  yields a selection efficiency of 92.5% and a false positive rate of 1.1%. Panel (c) shows the corresponding images, distinguishing true positives, i.e. out-of-domain samples from the “Striped” class in the Textures dataset, from false positives and reference samples from ImageNet. Notably, the reference images selected above the threshold exhibit striped patterns, suggesting that this concept was implicitly learned by ResNet50 despite the absence of explicit supervision. Interestingly, ResNet50 classifies the centroids of components  $f_1$  and  $f_4$  both as “zebra”, although their locations and the sign of their correlations with anomalies in logit space differ, indicating that the novel “Striped” concept overlaps only partially with the known “zebra” representation, and relates to other known classes such as “tiger”, “velvet” and “dishrag”.

*e) Extracting insights on intruded text:* Finally, Figure 11 summarizes the interpretability study performed on the language application we presented in Section IV-D. Panel (a) displays a simple 2D PCA projection of the data, where anomalous samples (yellow dots) overlap with nominal points, indicating that simple linear projections cannot separate them. In contrast, panel (b) shows a 2D projection derived from the most activated SPARKER components, where the anomalous points are distinctly isolated. Panel (c) presents the distribution of the anomaly score over the inspected data (black histogram) as opposed to the typical behavior of anomaly-free realizations (light blue bars); we identify a group of highly anomalous points (in the black box) for further analysis. The activation patterns of the most anomalous data points are displayed in panel (d), and their corresponding text lines in panel (e). We recognize two dominant patterns, highlighted in different colors in panel (e), corresponding to the activation of components  $f_0$  and  $f_4$ , respectively. Both patterns reveal over-represented linguistic expressions. In the light blue group, associated with  $f_4$ , we recognize the repeated use of the phrase “*Poca sapienza è*” (“little wisdom is”) at the beginning of each line, a construction entirely absent in the Divine Comedy. In the dark blue group, we identify the recurrent phrase “*E come quei che*” (“and like those who”) at the line openings. This expression does appear in the Divine Comedy in the form

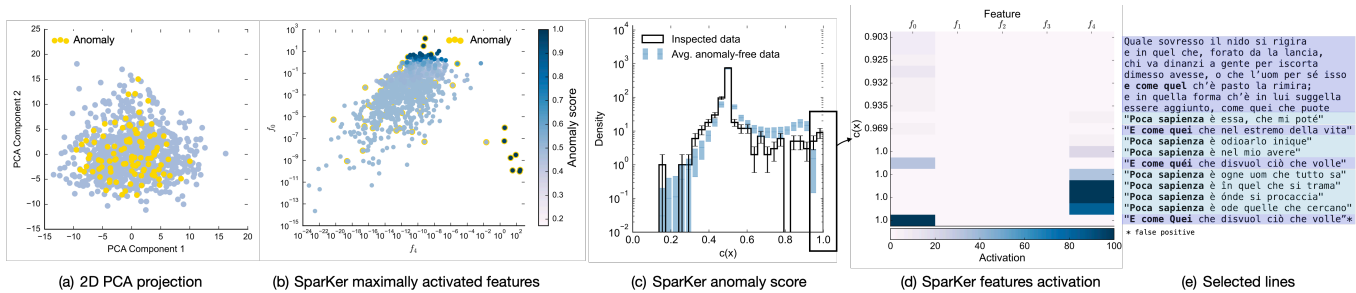


**Fig. 11: Inspecting detected intrusions in text lines.** (a) 2D principal component analysis (PCA) projection of the data, where the anomalous points, highlighted in yellow, lie on the support of the normal data. (b) 2D projection obtained using the two maximally-activated features found by SparKer; in contrast to PCA, SPARKER. finds low-dimensional representations that single out the most anomalous regions of the data. (c) Distribution of the anomaly score output by SPARKER. over the inspected data (black histogram), compared to the average expected distribution in absence of anomalies (the light blue bars measure the standard deviation over 100 anomaly-free realizations). (d) Activation pattern of SparKer’s components for the most anomalous data points. Two components,  $f_0$  and  $f_4$ , exhibit the most correlation with the anomaly score. (e) Most anomalous lines colored by their activation pattern.

marked by an asterisk at the bottom of the list, but the LLM generates multiple variations with hallucinated continuations.

## VI. FINAL REMARKS

SPARKER. unites sparsity, locality, and competition into a self-organizing ensemble for interpretable in-distribution anomaly detection. We demonstrated that SPARKER. reliably identifies subtle deviations across applications ranging from scientific discovery and generative-model validation to intrusion and open-world novelty detection, spanning diverse data modalities, feature-space dimensions, and signal fractions. In the most challenging regimes, SPARKER. consistently outperforms state-of-the-art two-sample tests. Beyond its detection power, SPARKER. naturally lends itself to interpretability: its components specialize to distinct regions of the data space, yielding a geometric decomposition of the anomaly score assigned to each input. This property paves the way for trustworthy, rule-based anomaly triggers, scientific insight extraction, and continual learning. SPARKER. demonstrates the importance of careful design choices and desiderata to control the failure modes of AD methods and to characterize the conditions under which we can expect them to succeed. Furthermore, SPARKER. highlights an interplay between properties of data representations and properties of statistical methods. We observed how rich and informative data representations endowed with meaningful geometry can enable successful, signal-agnostic detection.

The design of SPARKER. leaves open several exciting directions of future advances, from adaptive kernel covariances to trainable log-concave alternatives to Gaussian kernels [85].

While we focused on semi-supervised anomaly detection, the model’s capacity to capture local geometric structure suggests broader potential [86]. Future work will explore local activation mechanisms as a foundation for robust and interpretable model design beyond anomaly detection, advancing the integration of locality, interpretability, and adaptability in modern machine learning systems.

Finally, a question we have left unanswered is that of what constitute “good” feature extractors for anomaly detection? We conjecture that “good” feature extractors make it simple to relate anomalies in representation space back to attributes of inputs, suggesting some form of invertibility as important.

## ACKNOWLEDGMENT

G.G., S.B.T., and P.H. acknowledge the financial support of the National Science Foundation under Cooperative Agreement PHY-2019786 (The NSF AI Institute for Artificial Intelligence and Fundamental Interactions, <http://iaifi.org/>). D.B. and T.F. acknowledge the gift from the Chan Zuckerberg Initiative Foundation to establish the Kempner Institute for the Study of Natural and Artificial Intelligence at Harvard University. Computations in this paper were run on the FASRC Cannon cluster supported by the FAS Division of Science Research Computing Group at Harvard University.

APPENDIX A  
MODEL DESIGN AND IMPLEMENTATION

In this Section we provide additional details on the model design and implementation.

*A. Deterministic annealing*

The vanishing gradient represents the main engineering challenge to train local kernels. We mitigate this issue by imposing deterministic annealing to the kernels' width. Starting from a wide width,  $\sigma_0$ , we linearly reduce the kernels' width up to a final narrow width,  $\sigma_T$ , taking equally large steps at each epoch  $t$ :

$$\sigma_t = \sigma_0 + (\sigma_0 - \sigma_T) \cdot \frac{t}{T} \quad (15)$$

*B. Amplitude regularization for a robust testing*

When statistical power is low, density estimates are sensitive to fluctuations, leading to model misspecification and overfitting in sparse regions. Huber's seminal work on robust hypothesis testing [87] showed that minimax-optimal tests under distributional uncertainty clip the likelihood ratio to limit sensitivity to outliers. Following this principle, we clip SPARKER's kernel amplitudes as a regularization against noisy regions, with the clipping coefficient tuned in a signal-agnostic way using anomaly-free data. We further apply standard L2 regularization.

*C. Model initialization*

The kernels' amplitudes are initialized at zero, making the starting model identically null in all the data domain. This initialization reduces initial bias towards specific solutions and allows a slow evolution towards meaningful solutions as the widths are annealed. The width range for annealing is defined estimating the typical range of pair-wise distance between points. We compute the 1% and 99% percentiles of the empirical distribution of the pair-wise distance between data points (a subset of the data is used for computational reasons). The initial width is set at twice the 99% percentile, while the final width is set at half the 1% percentile. The kernels' locations are randomly initialized among the locations of the data points. This is an inexpensive way to ensure that the kernels are initially located in-distribution. This initialization, combined with the range chosen for the kernels' widths ensures with high probability that at least one model gradient is significantly larger than zero for each data point.

*D. Multiple resolution test*

Multiple solutions based on different values of the kernels' width can be retrieved from intermediate stages of the annealing process happening during training. A priori there is no way to tell which value of the width encountered during annealing is optimal for testing, as the latter depends on the specifics of the anomalous signal. To obtain robustness against scale variations, we perform multiple testing across values of the width and account for the trial factor by combining the resulting p-values into a single test. Based on previous studies on multiple testing with the NP test [88], the aggregation rule we adopt is the average of the minimum p-value and product of p-values [17]. For an observed value of the test,  $t_{\text{obs}}$ , the p-value is estimated empirically, as

$$\hat{p}_{\text{obs}} = \frac{1}{N_{\text{toys}}^{(H_0)} + 1} \left[ \sum_{i=1}^{N_{\text{toys}}^{(H_0)}} \mathbb{I}(t_i - t_{\text{obs}}) + 1 \right], \quad (16)$$

where  $\{t_i\}_{i=1}^{N_{\text{toys}}^{(H_0)}}$  represents a collection of anomaly-free realizations used for calibration.

APPENDIX B  
THEORETICAL ANALYSIS

In this appendix, we develop the theoretical underpinnings of SPARKER's anomaly detection properties. We restate and prove results included in Section III. The Neyman-Pearson (NP) loss which is optimized to train the SPARKER model is defined as:

$$L_{\text{NP}}[f] = \sum_{x \in \mathcal{R}} w_{\mathcal{R}}(e^{f(x)} - 1) - \sum_{x \in \mathcal{D}} f(x). \quad (17)$$

The dynamics of mean  $\mu_i$  and amplitude  $a_i$  are given by gradient descent on the NP Loss:

$$\mu_{i;t+1} = \mu_{i;t} - \eta \left. \frac{\partial L_{\text{NP}}[f_{\theta}]}{\partial \mu_i} \right|_{\theta=\theta_t}, \quad (18)$$

$$a_{i;t+1} = a_{i;t} - \eta \left. \frac{\partial L_{\text{NP}}[f_{\theta}]}{\partial a_i} \right|_{\theta=\theta_t}, \quad (19)$$

where  $\theta_t = \{\boldsymbol{\mu}_{1;t}, \dots, \boldsymbol{\mu}_{M;t}, a_{1;t}, \dots, a_{M;t}\}$  represents all trainable parameters at training iteration  $t$ . The loss function  $L_{\text{NP}}$  includes evaluating the model  $f$  at multiple data points  $\mathbf{x} \in \mathcal{R} \cup \mathcal{D}$ . We focus our analysis on the dynamics of the location  $\boldsymbol{\mu}_i$  and amplitude  $a_i$  of a generic kernel  $i$  in the SPARKER ensemble.

#### A. Effect of individual points on kernel means and amplitudes.

We first study the effect of individual data points on the dynamics of mean  $\boldsymbol{\mu}_i$  and amplitude  $a_i$  through their corresponding gradients  $\partial_{\boldsymbol{\mu}_i} f$ , and  $\partial_{a_i} f$  in the following lemma:

**Lemma 4** (Radial influence of points on kernels' location). *Individual points  $x$  impose a radial influence on kernel means  $\boldsymbol{\mu}_i$ , expressed as a vector field:*

$$\partial_{\boldsymbol{\mu}_i} f(\mathbf{x}) = A_i(\mathbf{x}) \cdot \mathbf{r}_i$$

where  $\mathbf{r}_i = \mathbf{x} - \boldsymbol{\mu}_i$  and  $A_i(\mathbf{x}) = \frac{1}{\sigma^2} \cdot [2a_i k_{\boldsymbol{\mu}_i}^\sigma(\mathbf{r}_i) - f_M^\sigma(\mathbf{x})] \cdot p^i[k_{\boldsymbol{\mu}_i}^\sigma(\mathbf{r}_i)]$ .

*Proof.* This is a direct consequence of our modeling choice, elaborated below.  $f$  is parameterized using Gaussian kernels, i.e.  $f(\mathbf{x}) \equiv f(\|\mathbf{r}_1\|^2, \dots, \|\mathbf{r}_M\|^2)$  with  $\mathbf{r}_i = \mathbf{x} - \boldsymbol{\mu}_i$ , thus  $\partial_{\boldsymbol{\mu}_i} f = (\partial_{\|\mathbf{r}_i\|^2} f) \cdot (-2\mathbf{r}_i)$  through the chain rule. The amplitude  $A_i$  is obtained by directly computing the gradient of  $f$  using the product rule.  $\square$

The radial influence of each data point can either be attractive (radially toward the point) or repulsive (radially away from the point) on the kernel mean  $\boldsymbol{\mu}_i$ . The conditions which determine the direction of influence are specified in the following lemma.

**Lemma 5** (Push-pull dynamic of kernels). *The dynamics of the  $i^{\text{th}}$  kernel location  $\boldsymbol{\mu}_i$  is the result of radial forces arising from the training points. Let  $y$  be the class label associated with each data point ( $y = 0$  for  $\mathbf{x} \in \mathcal{R}$  and  $y = 1$  for  $\mathbf{x} \in \mathcal{D}$ ), and let  $A_i(\mathbf{x}) = 2a_i k_i(\mathbf{x}) - f(\mathbf{x})$  the  $i^{\text{th}}$  be the kernel ‘‘mass charge’’ in  $\mathbf{x}$ . The sign of each interaction is determined as follows:*

$$\begin{aligned} \text{‘‘radially attractive’’} & \quad \text{if } A_i(\mathbf{x}) \cdot (2y - 1) > 0 \\ \text{‘‘radially repulsive’’} & \quad \text{if } A_i(\mathbf{x}) \cdot (2y - 1) < 0 \end{aligned}$$

*Proof.* The dynamics of kernel means is given by Eq. 19. For a generic parameter  $\theta = \{\boldsymbol{\mu}_i, a_i\}$ , the gradient of NP Loss (Eq. 17) is given as:

$$\partial_{\theta} L_{\text{NP}}[f_{\theta}] = w_{\mathcal{R}} \sum_{\mathbf{x} \in \mathcal{R}} e^{f_{\theta}(\mathbf{x})} \partial_{\theta} f_{\theta}(\mathbf{x}) - \sum_{\mathbf{x} \in \mathcal{D}} \partial_{\theta} f_{\theta}(\mathbf{x}), \quad (20)$$

while the parameter update through gradient descent is along the negative gradient of the loss (Eq. 19):

$$\Delta\theta = \theta_{t+1} - \theta_t \propto -\partial_{\theta} L_{\text{NP}}. \quad (21)$$

Therefore, for points  $\mathbf{x} \in \mathcal{R}$ ,  $\partial_{\theta} L_{\text{NP}}[f_{\theta}]$  and  $\partial_{\theta} f_{\theta}(\mathbf{x})$  have the same sign, while for  $\mathbf{x} \in \mathcal{D}$ ,  $\partial_{\theta} L_{\text{NP}}[f_{\theta}]$  and  $\partial_{\theta} f_{\theta}(\mathbf{x})$  have the opposite sign. The overall effect of  $\partial_{\theta} f$  on  $\Delta\theta$  can be captured by multiplying  $\partial_{\theta} f$  with the term  $(2y - 1)$  where  $y = \begin{cases} 0 & \mathbf{x} \in \mathcal{R}, \\ 1 & \mathbf{x} \in \mathcal{D} \end{cases}$ , since this induces an overall sign flip for points  $\mathbf{x} \in \mathcal{R}$ . Additionally, the multiplier of the gradient, denoted as  $A_i(\mathbf{x})$  above, can itself be positive or negative, and is determined by the kernel amplitudes, values and result of softmax weighting. Radially attractive behavior results when  $\Delta\boldsymbol{\mu}_i \propto \mathbf{r}_i = \mathbf{x} - \boldsymbol{\mu}_i$ , while repulsive behavior results when  $\Delta\boldsymbol{\mu}_i \propto -\mathbf{r}_i = \boldsymbol{\mu}_i - \mathbf{x}$ . The result for kernel location follows from the above using the gradient expression from Lemma 4.  $\square$

#### B. Kernel dynamics are affected only by nearby data points.

Having studied the effect of individual data points on parameter updates, we now turn to the question of which points from the data significantly affect the dynamics of kernel means. We show that only those data points that are within a neighborhood of the kernel mean  $\boldsymbol{\mu}_i$  can contribute to the dynamics of  $\boldsymbol{\mu}_i$ . Furthermore, this neighborhood is dependent on the scale  $\sigma$ . We first setup useful definitions:

**Definition 2** (Kernel radial  $\alpha$ -level). *Let  $k : \mathbb{R}_+ \rightarrow \mathbb{R}_+$  be a continuous, radial kernel profile that is nonincreasing in  $r \geq 0$  (i.e.  $k(r_1) \geq k(r_2)$  for  $r_1 \leq r_2$ ). For a given level  $\alpha \in (0, k(0))$  define the radial  $\alpha$ -level  $r_{\alpha}$  as the radius such that  $k(r) < \alpha \quad \forall r > r_{\alpha}$ , or equivalently  $r_{\alpha} = \sup\{r \geq 0 : k(r) \geq \alpha\}$ .*

By monotonicity of  $k$ , the set  $\{r \geq 0 : k(r) \geq \alpha\}$  is an interval  $[0, r_{\alpha}]$  (possibly closed or half-open), so  $r_{\alpha}$  is well defined.

For the Gaussian profile  $k(r) = \exp(-r^2/(2\sigma^2))$ , the level-set quantile admits the closed form  $r_{\alpha} = \sigma\sqrt{-2\ln\alpha}$ , valid for  $0 < \alpha < 1$ .

Using a kernel's radial  $\alpha$ -level, we show that each kernel has a *sphere of influence* which characterizes the region in space where data points can significantly affect the dynamics of kernel mean  $\mu_i$  and amplitude  $a_i$ .

**Lemma 6 (Kernel's Sphere of Influence).** *For each kernel  $i$  there exists a value  $\alpha \in [0, 1]$  such that the associated ball  $S_i^\sigma(\alpha) = \{z \in \mathbb{R}^d : \|z - \mu_i\| \leq r_{\alpha,i}^\sigma\}$  contains all the training points that contribute at least  $\epsilon_\alpha$  to the kernel's dynamics, i.e., points outside this ball have no more than  $\epsilon_\alpha$  effect on the kernel's dynamics:*

$$\exists \epsilon_\alpha > 0 \quad \text{s.t.} \quad |\partial_{\theta_i} f(z)| \leq \epsilon_\alpha \quad \forall z \notin S_i^\sigma(\alpha) \quad \text{with} \quad \theta_i \in [\mu_i, a_i] \quad (22)$$

where a small tail probability  $\alpha \ll 1$  implies a smaller gradient contribution outside the sphere of influence  $\epsilon_\alpha \ll 1$ . We name the ball  $S_i^\sigma(\alpha)$  the kernel's "Sphere of Influence". The dynamics of kernels is thus local on a scale that is determined by the kernels' width,  $\sigma$ , through the radial  $\alpha$ -level  $r_\alpha^\sigma$ .

*Proof.* (Kernel amplitude) The gradient of  $f$  with respect to  $a_i$  is given by:

$$\partial_{a_i} f(\mathbf{x}) = p_i[\mathbf{k}_\mu^\sigma] \cdot k_{\mu_i}^\sigma(\mathbf{r}_i) \quad (23)$$

Since  $p_i[\mathbf{k}_\mu^\sigma] \in [0, 1]$  and for  $\mathbf{x} \notin S_i(\alpha)$   $k_{\mu_i}^\sigma(\mathbf{r}_i) \in [0, \alpha]$ , we can write the following bound:

$$0 \leq \partial_{a_i} f(\mathbf{x}) \leq \alpha. \quad (24)$$

Choosing  $\epsilon_\alpha = \alpha$  gives us the desired result for kernel amplitudes.

(Kernel mean). Consider now the gradient of  $f$  with respect to kernel mean  $\mu_i$  (from Lemma 4):

$$\partial_{\mu_i} f(\mathbf{x}) = A_i(\mathbf{x}) \cdot \mathbf{r}_i, \quad (25)$$

$$A_i(\mathbf{x}) = \frac{1}{\sigma^2} \cdot [2 a_i k_{\mu_i}^\sigma(\mathbf{x}) - f_M^\sigma(\mathbf{x})] \cdot p^i[\mathbf{k}_\mu^\sigma](\mathbf{r}_i). \quad (26)$$

The coefficient  $A_i(\mathbf{x})$  determines the contribution of the point  $\mathbf{x}$  to the gradient  $\partial_{\mu_i} L_{NP}$  driving the dynamics of  $\Delta\mu_i$ . Since  $A_i(\mathbf{x})$  is the result of the product of three terms, we bound it by obtaining upper bounds on each term separately.

Consider a point  $\mathbf{x} \notin S_i^\sigma(\alpha)$ .

The factor  $\frac{1}{\sigma^2}$  does not depend on  $\mathbf{x}$  and is positive and bounded (design choice).

The factor  $[2 a_i k_{\mu_i}^\sigma(\mathbf{x}) - f_M^\sigma(\mathbf{x})]$  depends on  $k_{\mu_i}^\sigma(\mathbf{x})$  and  $f_M^\sigma(\mathbf{x})$ . From the definition of the set  $S_i^\sigma(\alpha)$ ,

$$\mathbf{x} \notin S_i^\sigma(\alpha) \implies \|\mathbf{x} - \mu_i\| > r_{\alpha,i}^\sigma. \quad (27)$$

Since  $r_{\alpha,i}^\sigma$  is the radial  $\alpha$ -level (Def. 2), most of the volume of  $k_{\mu_i}^\sigma$  is contained within the  $\alpha$ -level

$$\|\mathbf{x} - \mu_i\| > r_{\alpha,i}^\sigma \implies k_{\mu_i}^\sigma(\mathbf{x}) \leq \alpha. \quad (28)$$

To estimate the contribution of the terms  $f_M^\sigma$  and  $p_i[\mathbf{k}_\mu^\sigma]$  which include all kernels, we consider whether the chosen point  $\mathbf{x}$  belongs to the sphere of influence of other kernels. Consider two mutually exhaustive cases:

- *Case 1.* The point  $\mathbf{x}$  is outside the sphere of influence of all kernels:

$$\mathbf{x} \notin S_j^\sigma(\alpha) \quad \forall j \implies k_{\mu_j}^\sigma(\mathbf{x}) < \alpha \quad \forall j \quad (29)$$

We can write the following decomposition of  $f$ :

$$f(\mathbf{x}) = \sum_{j \in J^+} |a_j| \frac{k_j^2(\mathbf{x})}{\sum_{i \in J} k_i(\mathbf{x})} - \sum_{j \in J^-} |a_j| \frac{k_j^2(\mathbf{x})}{\sum_{i \in J} k_i(\mathbf{x})} \quad (30)$$

where  $J^+$  and  $J^-$  represent the subsets of indices in  $J = (1, \dots, M)$  corresponding to positive and negative amplitudes respectively:

$$J^+ = \{j \in J \mid a_j > 0\} \quad (31)$$

$$J^- = \{j \in J \mid a_j < 0\}. \quad (32)$$

$$(33)$$

We can write the following bound on  $f$ :

$$- \sum_{j \in J^-} |a_j| \frac{k_j^2(\mathbf{x})}{\sum_{i \in J} k_i(\mathbf{x})} \leq f \leq \sum_{j \in J^+} |a_j| \frac{k_j^2(\mathbf{x})}{\sum_{i \in J} k_i(\mathbf{x})}. \quad (34)$$

Using Eq. 29 and the fact that  $p_j \leq 1 \quad \forall j \in J$  this bound can be further developed in

$$-\alpha \sum_{j \in J^-} |a_j| \leq f(\mathbf{x}) \leq \alpha \sum_{j \in J^+} |a_j|. \quad (35)$$

Eq. 35 can be used to bound the expression  $[2a_i k_i(\mathbf{x}) - f(\mathbf{x})]$ :

$$2a_i k_i(\mathbf{x}) - \alpha \sum_{j \in J^+} |a_j| \leq 2a_i k_i(\mathbf{x}) - f(\mathbf{x}) \leq 2a_i k_i(\mathbf{x}) + \alpha \sum_{j \in J^-} |a_j|. \quad (36)$$

and because  $k_i(\mathbf{x}) < \alpha$  we can further develop into two cases:

$$-\alpha \sum_{j \in J^+} |a_j| \leq 2a_i k_i(\mathbf{x}) - f(\mathbf{x}) \leq \alpha(2|a_i| + \sum_{j \in J^-} |a_j|) \quad \text{if } a_i > 0 \quad (37)$$

$$-\alpha(-2|a_i| + \sum_{j \in J^+} |a_j|) \leq 2a_i k_i(\mathbf{x}) - f(\mathbf{x}) \leq \alpha \sum_{j \in J^-} |a_j| \quad \text{if } a_i < 0 \quad (38)$$

Since  $p_i \leq 1$  is bounded, this results suffices to say that  $A_i$  tends to zero linearly with  $\alpha$ .

- *Case 2.* The point  $\mathbf{x}$  lies in the sphere of influence of at least one other kernel  $j \neq i$ .

In this case we can decompose  $f$  as follows:

$$f(\mathbf{x}) = a_j \frac{k_j^2(\mathbf{x})}{\sum_{i \in J} k_i(\mathbf{x})} + \sum_{k \neq j, k \in J^+} |a_k| \frac{k_k^2(\mathbf{x})}{\sum_{i \in J} k_i(\mathbf{x})} - \sum_{k \neq j, k \in J^-} |a_k| \frac{k_k^2(\mathbf{x})}{\sum_{i \in J} k_i(\mathbf{x})} \quad (39)$$

Using the arguments in Case 1 for all  $k \neq j$  we can write the following bound:

$$2a_i k_i(\mathbf{x}) - \alpha \sum_{k \neq j, k \in J^+} |a_k| \leq 2a_i k_i(\mathbf{x}) - f(\mathbf{x}) + a_j \frac{k_j^2(\mathbf{x})}{\sum_{i \in J} k_i(\mathbf{x})} \leq 2a_i k_i(\mathbf{x}) + \alpha \sum_{k \neq j, k \in J^-} |a_k|. \quad (40)$$

In this case, we can distinguish between four cases depending on  $a_i$  and  $a_j$  signs:

$$-|a_j| \frac{k_j^2(\mathbf{x})}{\sum_{i \in J} k_i(\mathbf{x})} - \alpha \sum_{k \neq j, k \in J^+} |a_k| \leq 2a_i k_i(\mathbf{x}) - f(\mathbf{x}) \leq \alpha \left( 2|a_i| + \sum_{k \neq j, k \in J^-} |a_k| \right) \quad \text{if } a_i, a_j > 0 \quad (41)$$

$$-\alpha \sum_{k \neq j, k \in J^+} |a_k| \leq 2a_i k_i(\mathbf{x}) - f(\mathbf{x}) \leq \alpha \left( 2|a_i| + \sum_{k \neq j, k \in J^-} |a_k| \right) + |a_j| \frac{k_j^2(\mathbf{x})}{\sum_{i \in J} k_i(\mathbf{x})} \quad \text{if } a_i > 0, a_j < 0 \quad (42)$$

$$-|a_j| \frac{k_j^2(\mathbf{x})}{\sum_{i \in J} k_i(\mathbf{x})} - \alpha \left( -2|a_i| + \sum_{k \neq j, k \in J^+} |a_k| \right) \leq 2a_i k_i(\mathbf{x}) - f(\mathbf{x}) \leq \alpha \sum_{k \neq j, k \in J^-} |a_k| \quad \text{if } a_i < 0, a_j > 0 \quad (43)$$

$$-\alpha \left( \sum_{k \neq j, k \in J^+} |a_k| - 2|a_i| \right) \leq 2a_i k_i(\mathbf{x}) - f(\mathbf{x}) \leq \alpha \sum_{k \neq j, k \in J^-} |a_k| + |a_j| \frac{k_j^2(\mathbf{x})}{\sum_{i \in J} k_i(\mathbf{x})} \quad \text{if } a_i, a_j < 0. \quad (44)$$

Due to the term  $|a_j| \frac{k_j^2(\mathbf{x})}{\sum_{i \in J} k_i(\mathbf{x})}$ , the quantity  $2a_i k_i(\mathbf{x}) - f(\mathbf{x})$  remains finite as  $\alpha$  tends to zero:

$$-|a_j| \frac{k_j^2(\mathbf{x})}{\sum_{i \in J} k_i(\mathbf{x})} \leq 2a_i k_i(\mathbf{x}) - f(\mathbf{x}) \leq |a_j| \frac{k_j^2(\mathbf{x})}{\sum_{i \in J} k_i(\mathbf{x})} \quad \text{for } \alpha \ll 1. \quad (45)$$

We now study the SoftMax activation  $p_i(\mathbf{x}) = \frac{k_i(\mathbf{x})}{\sum_{k \in J} k_k(\mathbf{x})}$ , contributing to  $A_i(\mathbf{x})$ . The numerator,  $k_i(\mathbf{x})$ , is less than  $\alpha$  since  $\mathbf{x} \notin S_i(\alpha)$ . The denominator can be decomposed as follows:

$$\sum_{k \in J} k_k(\mathbf{x}) = \sum_{k \neq j, k \in J} k_k(\mathbf{x}) + k_j(\mathbf{x}). \quad (46)$$

Since  $k_k(\mathbf{x}) > 0$  by definition and  $k_j(\mathbf{x}) > \alpha$  for  $\mathbf{x} \in S_j(\alpha)$ , we can write the following lower bound for the denominator:

$$\sum_{k \in J} k_k(\mathbf{x}) = \sum_{k \neq j, k \in J} k_k(\mathbf{x}) + k_j(\mathbf{x}) > k_j(\mathbf{x}). \quad (47)$$

Which translates in the following upper bound for  $p_i(\mathbf{x})$ :

$$0 < p_i(\mathbf{x}) < \frac{\alpha}{k_j(\mathbf{x})}. \quad (48)$$

All together:

$$-|a_j| \frac{k_j^2(\mathbf{x})}{\sum_{i \in J} k_i(\mathbf{x})} \cdot \frac{\alpha}{k_j(\mathbf{x})} \leq (2a_i k_i(\mathbf{x}) - f(\mathbf{x})) \cdot p_i(\mathbf{x}) \leq |a_j| \frac{k_j^2(\mathbf{x})}{\sum_{i \in J} k_i(\mathbf{x})} \cdot \frac{\alpha}{k_j(\mathbf{x})} \quad (49)$$

$$\implies -|a_j| \frac{k_j(\mathbf{x})}{\sum_{i \in J} k_i(\mathbf{x})} \cdot \alpha \leq (2a_i k_i(\mathbf{x}) - f(\mathbf{x})) \cdot p_i(\mathbf{x}) \leq |a_j| \frac{k_j(\mathbf{x})}{\sum_{i \in J} k_i(\mathbf{x})} \cdot \alpha \quad (50)$$

which tends to zeros linearly with  $\alpha$ .

Thus, in either case, the gradient  $\partial_{\mu_i} f$  is small if  $\mathbf{x} \notin S_i^\sigma(\alpha)$  and  $\alpha \ll 1$ , which completes the proof.  $\square$

Therefore, only training points within the sphere of influence of a kernel significantly affect the dynamics of its mean. We induce localization of kernels by scale annealing, i.e., we gradually decrease the value of the scale  $\sigma$  so that kernels become localized, which is formalized as follows:

**Lemma 7** (Scale annealing leads to localization). *Monotonically annealing the kernels scale  $\sigma$ , shrinks the size of the sphere of influence:*

$$\sigma_t < \sigma_{t-1} \implies \text{Vol } S_i^{\sigma_t}(\alpha) < \text{Vol } S_i^{\sigma_{t-1}}(\alpha),$$

resulting in a decrease in the number of data points that influence the dynamics of each kernel  $i$ .

*Proof.* The proof follows trivially from the sphere of influence being restricted to Euclidean balls  $S_i^\sigma(\alpha)$  around  $\mu_i$  with a radius that is proportional to  $\sigma$ . Decreasing  $\sigma$  leads to a shrinkage of the Euclidean balls, and therefore a shrinkage of the sphere of influence.  $\square$

As a consequence of annealing-induced localization, we empirically observe that kernel means in SPARKER enter a regime where a single data point lies within the sphere of influence. This point is typically an anomalous data point. In this regime, kernel mean  $\mu_i$  converges to the data point:

**Theorem 2** (Convergence within sphere of influence). *If  $S_i^{\sigma_t}$  contains only one data point that corresponds to statistical fluctuations  $\mathbf{x}^* \in \mathcal{D}$ , and kernel  $i$  dominates other kernels such that the softmax output  $p_i \approx 1$  (i.e., the vector is nearly one-hot), then  $\mu_i$  converges radially towards the anomaly, getting  $\epsilon$ -close to  $\mathbf{x}^*$  in  $O(\log 1/\epsilon)$  further steps.*

*Proof.* From Lemma 4, we know that the dynamics of  $\mu_i$  will be radially toward the point  $\mathbf{x}^*$ . Therefore, the dynamics becomes one-dimensional, along the line joining  $\mu_i$  (initial value) and  $\mathbf{x}^*$ . If the point  $\mathbf{x}^* \in \mathcal{D}$ , and the probability vector is one hot, the gradient of NP loss can be simplified as:

$$\partial_{\mu} L_{NP} \approx -f_t(\mathbf{x}^*) \left( \frac{\mathbf{x}^* - \mu_t}{\sigma^2} \right). \quad (51)$$

Plugging this into the gradient descent equation gives us,

$$\mu_{t+1} \approx \mu_t + \eta f_t(\mathbf{x}^*) \left( \frac{\mathbf{x}^* - \mu_t}{\sigma^2} \right), \quad (52)$$

$$\text{where } f_t(\mathbf{x}^*) = \exp\left(-\frac{\|\mathbf{x}^* - \mu_t\|^2}{2\sigma^2}\right). \quad (53)$$

Let  $\delta_t = \|\mu_t - \mathbf{x}^*\|$ . Subtracting  $\mathbf{x}^*$  from both sides of the above equation and writing everything in terms of  $\delta_t$  results in:

$$\delta_{t+1} \approx \delta_t - \eta \frac{\delta_t}{\sigma^2} \exp\left(-\frac{\delta_t^2}{2\sigma^2}\right). \quad (54)$$

If  $\delta_t/\sigma \ll 1$  (which can be achieved by initializing  $\sigma$  to a large value), the exponent can be approximated using the leading term in the Taylor series expansion as  $\exp\left(-\frac{\delta_t^2}{2\sigma^2}\right) \approx 1 - \frac{\delta_t^2}{2\sigma^2}$ , which gives us:

$$\delta_{t+1} \approx \delta_t - \eta \frac{\delta_t}{\sigma^2} \left(1 - \frac{\delta_t^2}{2\sigma^2}\right), \quad (55)$$

$$\approx \delta_t (1 - \eta/\sigma^2), \quad (56)$$

by retaining only the first order term since  $\delta_t/\sigma \ll 1$ . Iterating the above over time yields,

$$\delta_t \approx \delta_0 (1 - \eta/\sigma^2)^t. \quad (57)$$

This implies the following convergence result for  $\delta_t$ :

$$\text{for } \epsilon > 0, \delta_t \leq \epsilon \forall t \geq \frac{\log(\delta_0/\epsilon)}{\log\left(\frac{1}{1-\eta/\sigma^2}\right)}. \quad (58)$$

Since  $\delta_t = \|\mu_t - \mathbf{x}^*\|$ , the above result indicates that  $\mu_t$  converges  $\epsilon$ -close to  $\mathbf{x}^*$  in  $O(\log 1/\epsilon)$  steps of gradient descent (starting from when  $\mathbf{x}^*$  is the only point in the sphere of influence of kernel  $i$ ). This completes the proof.  $\square$

APPENDIX C  
SENSITIVITY ACROSS ANOMALY REGIMES

In-distribution detection can hit different levels of difficulty based on the degree of separability between the anomalies and the reference data, and based on the fraction of signal present in the dataset. In regions of high density of the reference, small signal injections are hard to detect because the log-density-ratio tends to be very close to zero. Whereas, in the tails of the reference distribution the anomalous pattern has to compete with statistical fluctuations.

We explore the sensitivity of SPARKER. as a function of the anomaly separability with a series of one- and two-dimensional toy experiments. In the experiments, a localized anomalous signal is injected at different levels of overlap with the reference, either in the bulk, the tail, or out of the distribution. The amount of signal injected is tuned to keep the detection hardness approximately constant in the various scenarios. In addition, we test SPARKER. in on non-localized signals mimicking domain shifts, for which the inductive biases encoded in the model are not optimal. The benchmarks are detailed in the following.

### A. 1D toy experiments

The first benchmark we consider is a one-dimensional toy model introduced in [37]. The data distribution under the reference model is a unit scale exponential. The data under the alternative hypotheses are composed of a mixture of reference-like data and signal-like data. To test the model ability under different separability regimes, we consider localized signals of Gaussian form with scale 0.16 and different locations, as well as a signal manifesting as an excess in the tail proportional to  $x^2 e^{-x}$ .

The number of expected events in the dataset  $N(\mathcal{R}) = 2000$ . The reference sample  $\mathcal{R}$  is taken 10 times larger than the expected number of events in the dataset  $N(\mathcal{R})$ ,  $N_{\mathcal{R}} = 20\,000$ .

The details on the signal injected are given in Table I.

	label	$\mu$	$\sigma$	$N(S)/N(\mathcal{R})$
<b>Gaussian bumps</b>	bulk	1.6	0.16	$4.5 \cdot 10^{-2}$
	tail	6.4	0.16	$5 \cdot 10^{-3}$
	extreme tail	9	0.16	$2.5 \cdot 10^{-3}$
<b>Tail excess</b>	excess			$4.5 \cdot 10^{-2}$

TABLE I: Summary of the 1D signal benchmarks.

### B. 2D mixture of Gaussians

The second benchmark that we consider is inspired by [67]. The ground truth is represented by a mixture of four 2D Gaussian models with covariance matrix  $\Sigma = 4 \cdot \mathbb{I}^{2 \times 2}$ , located at the corner of a square of length 16. We consider four anomalous scenarios. Two of them consist of a local new cluster appearing either in the bulk of the bottom left Gaussian or in the extreme tail of all of them (e.g. in the middle of the square identified by the four Gaussian models' locations). The others, inspired by [67], are a non-local distortions obtained varying the scale of the bottom left Gaussian. While the latter is a shape anomaly that doesn't modify the expected number of data points, the new anomalous clusters are an injection on top of a set of background-like data. To make the problem hard, we consider very low signal injections (1% or lower).

	label	$\mu$	$\sigma$	$N(S)/N(\mathcal{R})$
<b>Gaussian bumps</b>	bulk	(-6, -6)	1	$1 \cdot 10^{-2}$
	extreme tail	(0, 0)	1	$1 \cdot 10^{-3}$
<b>Scale distortion</b>	smearing		2.2	
	squeezing		1.8	

TABLE II: Summary of the 2D signal benchmarks.

Figure 12 shows the signal detection performances for each signal benchmark for a one-dimensional toy model where the reference distribution is exponential and a two-dimensional toy model resulting from the mixture of four Gaussians. The metric used to evaluate the sensitivity is the test power at 5% type I error, obtained calibrating empirically the test with anomaly-free experiments. We compare SPARKER. with Falcon and MMD (the number of kernels defining each model is reported in the figure legend after the dash).

When the signal is located in low density regions of the reference distribution, the detection performances of both Falcon (orange bars) and MMD (green bars) are significantly lower than what obtained with SPARKER. (blue bars). Moreover, the performance of SPARKER. tends to be high even for very small number of trainable parameters, suggesting that the sparsity assumption combined with locality are a good set of biases for this kind of problems. Interestingly, the model performances are competitive even for the non localized signals.

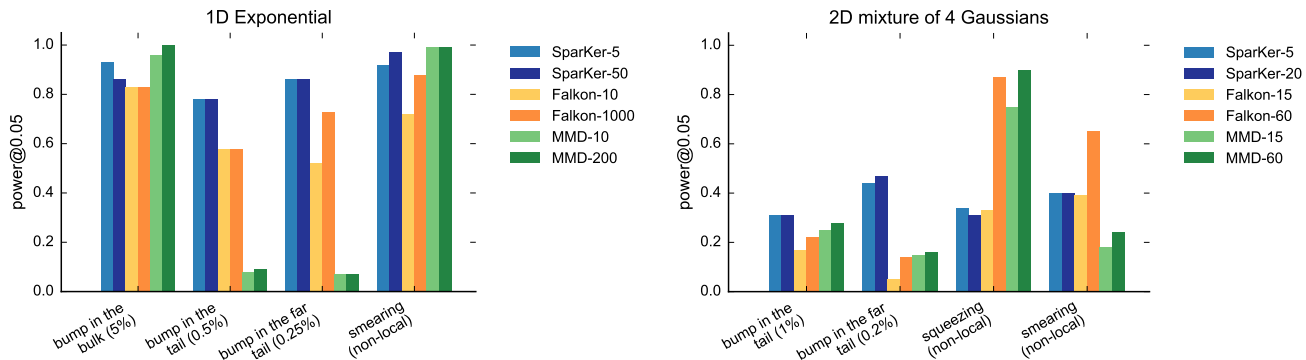


**Fig. 12: Sensitivity comparison across regimes of anomaly separability.** Summary plot on sensitivity studies with toys models. SPARKER. beats state-of-the-art algorithms on rare anomalies localized-in-distribution. The numbers in the labels refer to the number of kernel used in the implementation.

## APPENDIX D THE ROLE OF THE NP LOSS

We compare the gradients of three loss functions commonly considered for likelihood-ratio or two-sample learning: the Neyman–Pearson loss (NP), binary cross-entropy loss (BCE), and mean-squared error loss (MSE). Writing  $f(x)$  for the model logit and  $\sigma(f) = 1/(1 + e^{-f})$  for its logistic transformation, the losses and their gradients with respect to the model parameters are listed in Table III.

<b>NP</b>	$\mathcal{L}_{\text{NP}}[f] = w_{\mathcal{R}} \sum_{x \in \mathcal{R}} (e^{f(x)} - 1) - \sum_{x \in \mathcal{D}} f(x)$ $\partial_{\theta} \mathcal{L}_{\text{NP}}[f] = w_{\mathcal{R}} \sum_{x \in \mathcal{R}} e^{f(x)} \partial_{\theta} f(x) - \sum_{x \in \mathcal{D}} \partial_{\theta} f(x)$
<b>BCE</b>	$\mathcal{L}_{\text{BCE}}[f] = -w_{\mathcal{R}} \sum_{x \in \mathcal{R}} \log[1 - \sigma(f(x))] - \sum_{x \in \mathcal{D}} \log[\sigma(f(x))]$ $\partial_{\theta} \mathcal{L}_{\text{BCE}}[f] = w_{\mathcal{R}} \sum_{x \in \mathcal{R}} \sigma(f(x)) \partial_{\theta} f(x) - \sum_{x \in \mathcal{D}} [1 - \sigma(f(x))] \partial_{\theta} f(x)$
<b>MSE</b>	$\mathcal{L}_{\text{MSE}}[f] = w_{\mathcal{R}} \sum_{x \in \mathcal{R}} [\sigma(f(x))]^2 + \sum_{x \in \mathcal{D}} [1 - \sigma(f(x))]^2$ $\partial_{\theta} \mathcal{L}_{\text{MSE}}[f] = w_{\mathcal{R}} \sum_{x \in \mathcal{R}} 2 \sigma(f(x))^2 [1 - \sigma(f(x))] \partial_{\theta} f(x) - \sum_{x \in \mathcal{D}} 2 \sigma(f(x)) [1 - \sigma(f(x))]^2 \partial_{\theta} f(x)$

**TABLE III: Comparison of loss functions and their gradients.** We study the Neyman–Pearson (NP) loss, the Binary Cross Entropy (BCE) loss and the Mean Squared Error (MSE) loss. Each loss defines a different optimization landscape and gradient behavior.

The different loss definitions imply distinct gradient behaviors. The BCE and MSE losses depend on the function  $f$  through its logistic transformation. Thus, for the chain rule, their gradients depend on the sigmoid as well. In the MSE case, all the terms contributing to the gradient depend on the product  $\sigma(f) \cdot [1 - \sigma(f)]$ , producing rapid gradient decay as  $\sigma(f)$  approaches either 0 or 1, independently on the point  $x$  category. As for the BCE loss, contributions coming from the reference sample  $\mathcal{R}$  directly depend on the logistic factor  $\sigma(f)$ , whereas contributions coming from the data sample  $\mathcal{D}$  depend on the term  $[1 - \sigma(f)]$ . This structure causes partial gradient saturation when  $\sigma(f)$  approaches 1 for points in  $\mathcal{D}$  or 0 for points in  $\mathcal{R}$ . The result is a slower learning dynamic for confidently classified samples, though typically less severely than for MSE.

The NP loss does not depend on  $f$  through the logistic transformation, thus avoiding vanishing gradients typical of sigmoid-based losses. However, the loss is unbounded from below and requires implicit or explicit regularization, such as the activations clipping used in this work, to prevent divergence.

Due to its non-vanishing gradients, the NP loss seems the most suitable candidate in settings that require accurate learning of the density-ratio.

We validate these theoretical observation over a one-dimensional controlled experiment. We consider the scenario of a peak in the extreme tail of an exponential distribution, described in Section C-A. Table IV reports the detection power at 5% type I error for SPARKER. optimized using MSE, BCE or NP loss. As expected the MSE loss is the least effective choice and NP the most effective one.

Model	MSE loss	BCE loss	NP loss
Power@5%	0.61	0.68	<b>0.86</b>

TABLE IV: Caption

## APPENDIX E THE ROLE OF SOFTMAX ACTIVATION

In this section we further elaborate on the impact of SoftMax activation in the SPARKER design. Figure 13 illustrates the impact of SoftMax for a one-dimensional model composed of two kernels, located at  $\mu_1$  and  $\mu_2$  respectively. The left panel shows the model design with (dashed orange line) and without (solid blue line) SoftMax. The middle and right panels display the partial derivatives of the model with respect to the kernels' locations  $\mu_1$  and  $\mu_2$ , highlighting the implications of SoftMax on the learning dynamics affecting the kernels' locations. The presence of SoftMax activation causes a change of sign in the derivative with respect to one kernel for regions of the input space where the other kernel ‘‘wins’’ the competition, altering the direction of the kernel’s motion during the learning dynamics. The implications of this phenomenon is an increased model sensitivity to rare

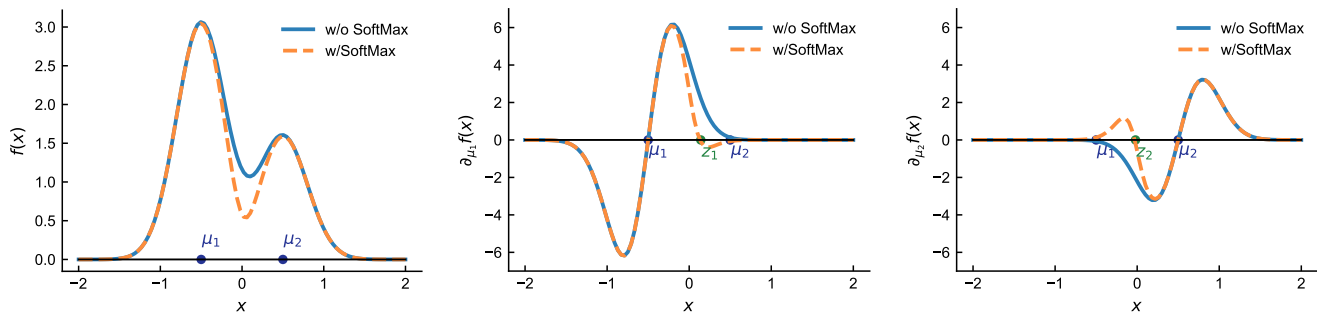


**Fig. 13: The effect of SoftMax on SPARKER. model.** We compare SPARKER in presence (dashed orange line) and in absence the (solid blue line) of SoftMax activation in a 1D scenario. The left panel shows an example of a 2-kernel model; the middle and right panels show the partial derivatives of the model with respect to the kernels’ locations  $\mu_1$  and  $\mu_2$ . The kernels interaction induced by SoftMax manifest as a change of sign in the derivative governing the direction of the kernels’ motion during the learning dynamics.

anomalies. Table V shows numerical results obtained comparing SPARKER with and without SoftMax activation for the one-dimensional problem of detecting rare anomalies on the extreme tails of the nominal distribution, introduced in Section C-A. SoftMax leads to a higher power of the Neyman–Pearson test statistic. This improvement is accompanied by a more uniform spatial allocation of kernels, as evidenced by the Moran spacing [89] in Figure 14. Together, these results indicate that SoftMax promotes a more efficient and homogeneous exploration of the input space, enhancing chances of discovery.

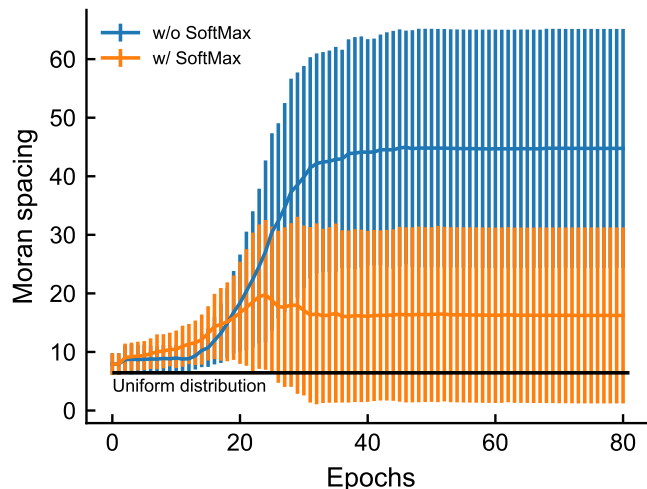
Model	w/o SoftMac	w/ SoftMax
Power@5%	0.72	<b>0.86</b>

TABLE V: Caption

## APPENDIX F APPLICATIONS DETAILS

### A. Gravitational waves detection

Gravitational waves are ripples in spacetime generated by massive accelerating objects, such as merging black holes or neutron stars, and propagate at the speed of light. Detectors like LIGO [90] directly measure these signals on Earth, revealing the properties of their sources and testing the nature of gravity. Many predicted sources remain unobserved, and the diversity of possible signals—often lacking precise theoretical models—motivates anomaly detection methods. In this work, we analyze data from the beginning of LIGO’s O3a run [91], [92], categorized into Gaussian noise, instrumental glitches, and six astrophysical or hypothetical source classes. Following the NSF HDR ML Challenge [6], we include white-noise bursts (WNB) as anomalies. Our study uses the feature-extraction pipeline of [21] to provide inputs to the SPARKER algorithm. A one-dimensional ResNet encoder setup as in [93] is fine-tuned using supervised contrastive learning on anomaly-free data to provide a four-dimensional compressed representation. For the presented experiments, we set the size of the reference sample at 20 000, and the size of the inspected data at 4 000. Signal injections range from 1 to 5%.



**Fig. 14: SoftMax improves specialization.** We measure the distance of the kernels distribution from a uniform distribution computing the Moran spacing statistics as a function of the training epoch. The Moran evolution for SPARKER, in absence of SoftMax activation is reported in blue, whereas the trend in presence of SoftMax is reported in orange. The solid lines are obtained averaging over 100 anomaly-free realizations; error bars represent the standard deviation. We focus on the 1-dimensional problem of detecting an extreme peak in the tail, introduced in Section C. The average value of the test statistics under uniform assumption is highlighted in black. Generally, the highest the value of Moran spacing the farther from uniformity assumption. On average including SoftMax in the model design leads to a more uniform distribution of kernels over the space.

### B. New particle jets discovery

In high energy physics, hadronic jets are sprays of particles originating from quarks or gluons produced in hadron collider experiments. Their substructure provides hints of the physics process underlying their generation, making them a valuable tool to search for new phenomena deviating from Standard Model of particle physics. We apply SPARKER to simulations of particle physics jets produced in proton-proton collisions at the Large Hadron Collider (LHC), available in the JETCLASS dataset [94], [95]. Jets originating from quarks and gluons (QCD), top quark decays ( $t \rightarrow bqq'$ ), and vector boson decays ( $V \rightarrow qq'$ ) are considered as background classes, representing the nominal generation model. Following the numerical experiments proposed in [21], we consider as a signal jets produced by the Higgs boson decaying to bottom-antibottom quark pairs. The encoder, introduced in [21], has the Particle Transformer (ParT) model as backbone [95], and an additional fully connected final layer to fine tune the embedding with supervised contrastive learning. For the experiments presented in the main paper, we set the size of the latent space at 128, the reference sample is 100 000 events, and the size of the inspected data Poisson fluctuates around 20 000. Signal events in this case are added to background events and range from 0.5 to 2% of the background. Also in this case, the total number fluctuates according to a Poisson distribution around the chosen working point value<sup>3</sup>.

### C. Hybrid butterfly discovery

Detecting hybrid species and assess their statistical significance at the population level is a crucial task to recognize the emergence of new species in evolutionary biology. We apply SPARKER to the NSF HDR ML Challenge of identifying new hybrids samples in collections of butterfly images [6]. The data are a subset of the Heliconius Collection (Cambridge Butterfly) consisting of butterfly images and corresponding labels identifying their nature (either hybrids or not) [96-119]. For the experiments presented in the main paper, we embed the data using the 1000-dimensional logits representation of a ResNet50 pretrained on ImageNet. Due to the limited amount of available data, the reference sample only contains 1 000 points, and the size of the inspected data 100. Signal injections range from 5 to 20% of the background.

### D. CIFAR-10 vs. CIFAR-5m

In the experiments involving generative model validation using CIFAR-10 and CIFAR-5m datasets, we consider the CIFAR-10 test set, composed of 10000 data points, as data  $\mathcal{D}$  and a 100000 size sample from CIFAR-5m as reference  $\mathcal{R}$ . Both samples are processed using ResNet50 pretrained on ImageNet to extract a 1000D representation to run SPARKER on. When performing bootstrap over anomaly-free realizations to calibrate the test we randomly sample both the reference and the data from a set of 300000 CIFAR-5m points.

<sup>3</sup>Poissonian fluctuations in the number of events in each class simulate real experimental conditions at colliders

### E. OOD in ImageNet

For the experiments involving out-of-domain detection in ImageNet, we consider data samples  $\mathcal{D}$  of 1000 points and compared them with a reference sample  $\mathcal{R}$  of size 10000. The data are a mixture of ImageNet data points and novelties, taken from the Striped class of the Texture dataset. The reference set is fully drawn from the ImageNet dataset and represent the close-world assumption. Both samples are processed using ResNet50 pretrained on ImageNet to extract a 1000D representation to run SPARKER on.

### F. Implementation details

In all applications considered in this paper we run a 5-kernel SPARKER. The model initialization follows the indications provided in Section A. The number of training epochs, the L2 regularization coefficient and the amplitude clip are independently chosen for each application to ensure good statistical behavior of the test in anomaly-free condition (i.e. calibration settings). We summarize the hyperparameter choice in Table VI. add the comparison with other loss functions and gradient calculations

Application	$n_{steps}$	L2 coeff.	Amplitude clip
Gravitational waves detection	100k	1	100
New particle jets discovery	100k	$10^{-3}$	100
Hybrid butterfly discovery	100k	$10^{-4}$	200
intrusion detection in Dante's text	100k	$10^{-3}$	500
OOD in ImageNet	40k	0	10k
CIFAR-10 vs. CIFAR-5m	40k	0	10k

**TABLE VI: SPARKER training details.** Number of training epochs, L2 regularization coefficient and amplitude clipping for various applications considered in the paper.

to motivate the loss design choice

## APPENDIX G IMPACT OF DATA DIMENSIONALITY

We study the impact of the data dimensionality on the detection performances, focusing on the problem of particle jets discovery. As detailed in Section F, the feature extraction employed in this application results from fine-tuning a transformer-based model tailored to analyze particle jets. We prepare different data representation scanning the size of the latent representation while keeping all other aspects of the training the same. Figure 15 shows the detection power at 5% false positive rate as a function of the size of the latent space for SPARKER and a selection of baselines. Beside MMD and Falkon, we implemented a distance-based test relying on the Mahalanobis metric [12], and the Fréchet Distance (FD), assuming normal distribution of the two samples [120]. Our experiments show stable performances for all tests except the Mahalanobis-based, which loses power as the number of dimensions increases. Falkon and SPARKER obtain the highest performances.

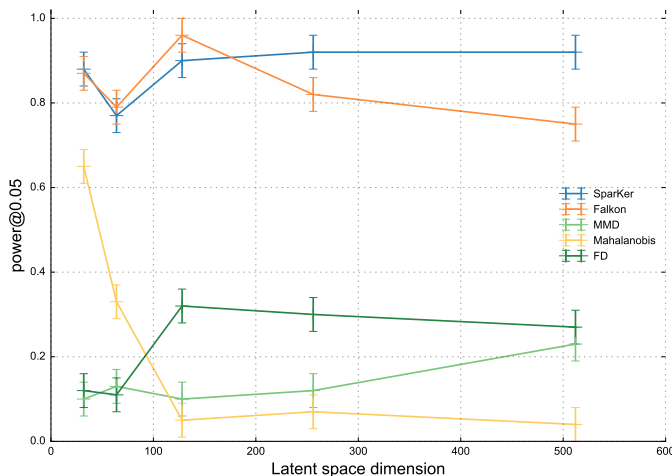


**Fig. 15: Impact of latent space size in particle jets discovery.** Detection power at 5% type I error as a function of latent space size. We focus on a 1% anomaly fraction. Each color represents a different detection method. The power and type I error are estimated using 100 realizations in anomaly conditions and 300 realizations anomaly-free. Error bars represent the Clopper-Person confidence interval. All methods except Mahalanobis have stable performances across dimension scan. The NP test, in both SPARKER and Falkon implementations, consistently provides the highest power.

APPENDIX H  
ADDITIONAL PLOTS ON INTERPRETABILITY

In this Section we report additional interpretability studies for the applications presented in the main paper.

*a) Interpreting discovered species of butterflies.:* The left side of Figure 16 showcases the result of a hybrid butterfly detection task. Panel (a) shows the distribution of the anomaly score across the inspected data in black compared to the average distribution in absence of signal in light blue (error bars represent the standard deviation over 100 anomaly-free realizations). SPARKER identifies three kernel components ( $f_1$ ,  $f_2$ , and  $f_4$ ) that are strongly activated by the most anomalous samples, two of which are positively correlated with the anomaly score (see panel (b)). By projecting data onto the subspace spanned by these two components, distinct regions of anomalous butterflies emerge—corresponding to specific phenotypic variations. For instance, butterflies in the upper-left region display two bright white spots on the upper wings, whereas those in the lower-right exhibit only one and an overall softer coloration.

*b) Interpreting statistical deviations in CIFAR AI generation.:* The outcome of the CIFAR generative model validation task is summarized on the right side of Figure 16. SPARKER reveals a consistent excess in the right tail of the anomaly score distribution reported in panel (d), indicating that the reference model under-represents certain regions of data space. The analysis of component activations highlights that all kernels are relevant, with  $f_1$ ,  $f_2$ , and  $f_3$  positively correlated with the anomaly score. Visualizing the three-dimensional space spanned by these components highlights distinct and nearly orthogonal anomaly clusters, which correspond to ImageNet categories such as “rule,” “pechines,” and “crossword puzzle.” Together, these results illustrate how SPARKER enables geometric and semantic interpretability across distinct application domains.

Anomalous butterflies laying at the edges of the distribution show different phenotypes: on the top left corner butterflies have two white stains on the top wings; on the bottom right corner butterflies only have one white stain and overall milder coloring.

APPENDIX I  
COMPUTING RESOURCES

The training of SPARKER is performed using code optimized for GPUs usage. Memory and time requirements depends on the size of the training set ( $N$ ), the number of kernels ( $M$ ), the size of the data space ( $d$ ), and the number of iterations ( $n_{\text{steps}}$ ). We summarize the average training time of our experiments in table VII. Errors correspond to standard deviation across 100 replicas.

Application	$N$	$M$	$d$	$n_{\text{steps}}$	time (s)
Gravitational waves	$24 \cdot 10^3$	5	4	$10^5$	$125 \pm 1$
Particle Jets	$60 \cdot 10^3$	5	128	$10^5$	$350.1 \pm 0.8$
Butterfly Hybrids	$1.1 \cdot 10^3$	5	1000	$10^5$	$1589 \pm 19$
Divine Comedy	$15 \cdot 10^3$	5	384	$10^5$	$269 \pm 0.9$
ImageNet OOD	$11 \cdot 10^3$	5	1000	$4 \cdot 10^4$	$3455 \pm 125$
CIFAR-10 vs. CIFAR-5m	$110 \cdot 10^3$	5	1000	$4 \cdot 10^4$	$33576 \pm 294$

**TABLE VII: Summary table of computing time on GPU.** We report the average computing time of a single SPARKER training (in seconds) for the various applications considered in this paper. For each applications we list the relevant parameters affecting the training time: size of training set ( $N$ ), number of SPARKER’s components ( $M$ ), number of dimensions of the data representation ( $d$ ) and number of iterations ( $n_{\text{steps}}$ ).

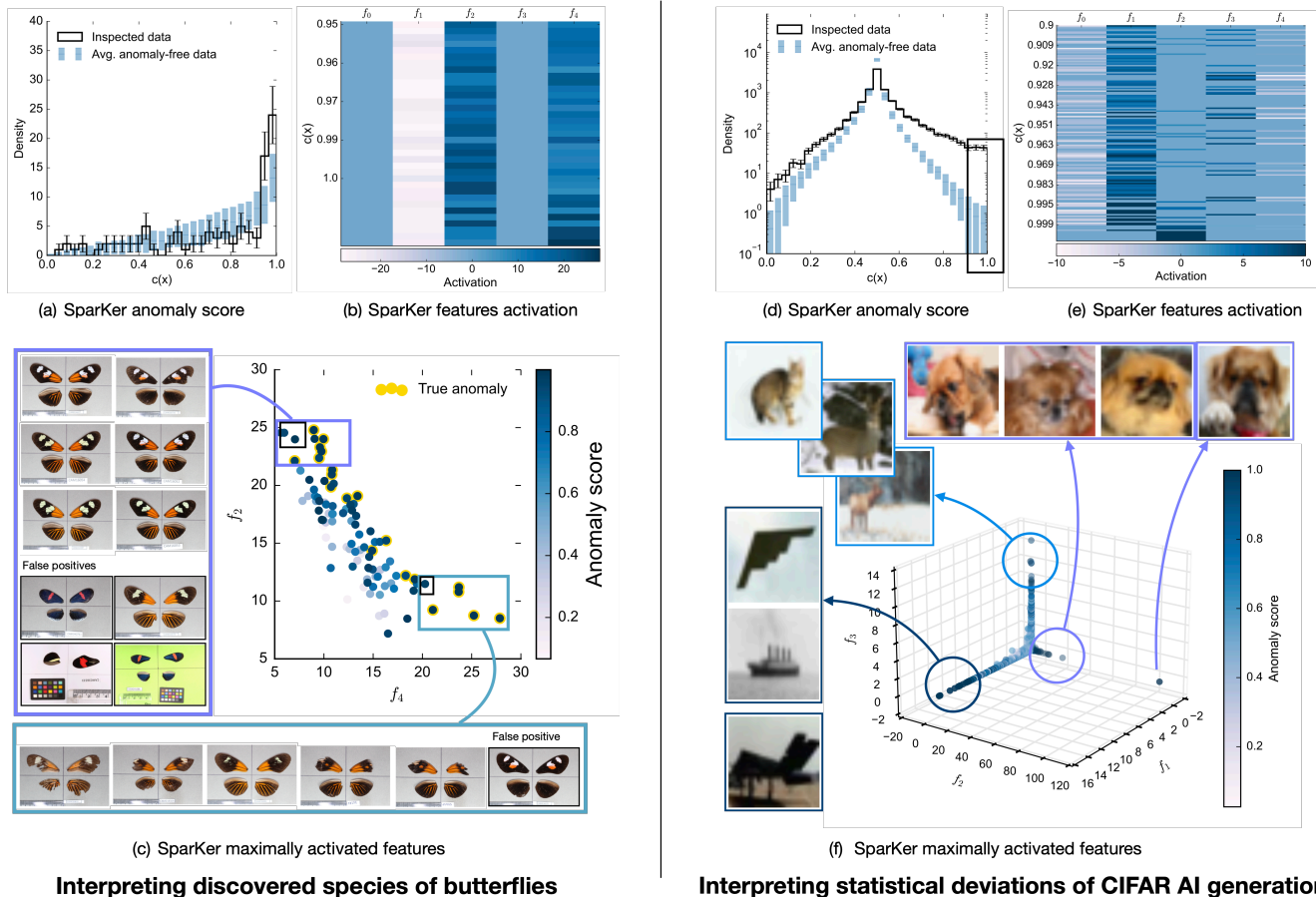


**Fig. 16: Extracting geometric interpretation from SPARKER.** The left side of the figure shows an example of data analysis in the hybrid butterfly detection problem. From panel (b) we identify two SPARKER components ( $f_2$  and  $f_4$ ) highly activated by the most anomalous points in the dataset. In panel (c) we report the correlation plot between such components, color coded by the anomaly score, and we distinguish groups of correctly identified hybrids according to their location in this plane. The right side of the figure shows the results of our experiments on the CIFAR generative model validation problem. Panel (d) shows a consistent excess in the right tail of the anomaly score distribution, telling that the generative model (used as the reference) fails to adequately represent a subspace of the data. More precisely, it under-represent it. Panel (e) informs us on the main regions of model misspecification; three components ( $f_1$ ,  $f_2$  and  $f_3$ ) highly activate to the anomalous points. Panel (f) shows a 3D scatter plot over these components, color coded by anomaly score, and identify three orthogonal subgroups of anomalies, aligning with the ImageNet classes of “rule” ( $f_1$ ), “pechinese” ( $f_2$ ), and “crossword puzzle” ( $f_3$ ).

## REFERENCES

- [1] V. Chandola, A. Banerjee, and V. Kumar, “Anomaly detection: A survey,” *ACM Comput. Surv.*, vol. 41, July 2009.
- [2] M. Lochner and B. A. Bassett, “Astronomy: Personalised active anomaly detection in astronomical data,” *Astronomy and Computing*, vol. 36, p. 100481, 2021.
- [3] P. U. Eze, N. Geard, I. Mueller, and I. Chades, “Anomaly detection in endemic disease surveillance data using machine learning techniques,” in *Healthcare*, vol. 11, p. 1896, MDPI, 2023.
- [4] V. Belis, P. Odagiu, and T. K. Aarrestad, “Machine learning for anomaly detection in particle physics,” *Reviews in Physics*, vol. 12, p. 100091, 2024.
- [5] I. Zingman, B. Stierstorfer, C. Lempp, and F. Heinemann, “Learning image representations for anomaly detection: Application to discovery of histological alterations in drug development,” *Medical Image Analysis*, vol. 92, p. 103067, 2024.
- [6] E. G. Campolongo, Y.-T. Chou, E. Govorkova, W. Bhimji, W.-L. Chao, C. Harris, S.-C. Hsu, H. Lapp, M. S. Neubauer, J. Namayanja, *et al.*, “Building machine learning challenges for anomaly detection in science,” *arXiv preprint arXiv:2503.02112*, 2025.
- [7] V. Moro, C. Loh, R. Dangovski, A. Ghorashi, A. Ma, Z. Chen, S. Kim, P. Y. Lu, T. Christensen, and M. Soljačić, “Multimodal foundation models for material property prediction and discovery,” *Newton*, vol. 1, no. 1, 2025.
- [8] A. Patcha and J.-M. Park, “An overview of anomaly detection techniques: Existing solutions and latest technological trends,” *Computer networks*, vol. 51, no. 12, pp. 3448–3470, 2007.
- [9] Y. Wu, B. Sicard, and S. A. Gadsden, “Physics-informed machine learning: A comprehensive review on applications in anomaly detection and condition monitoring,” *Expert Systems with Applications*, vol. 255, p. 124678, 2024.
- [10] F. Wang, Y. Jiang, R. Zhang, A. Wei, J. Xie, and X. Pang, “A survey of deep anomaly detection in multivariate time series: taxonomy, applications, and directions,” *Sensors (Basel, Switzerland)*, vol. 25, no. 1, p. 190, 2025.
- [11] D. O. Johnston, A. Chakraborty, and N. Belrose, “Mechanistic anomaly detection for” quirky” language models,” *arXiv preprint arXiv:2504.08812*, 2025.

- [12] A. Miyai, J. Yang, J. Zhang, Y. Ming, Y. Lin, Q. Yu, G. Irie, S. Joty, Y. Li, H. Li, *et al.*, “Generalized out-of-distribution detection and beyond in vision language model era: A survey,” *arXiv preprint arXiv:2407.21794*, 2024.
- [13] T. Ghosal, T. Saikh, T. Biswas, A. Ekbal, and P. Bhattacharyya, “Novelty detection: A perspective from natural language processing,” *Computational Linguistics*, vol. 48, pp. 77–117, 04 2022.
- [14] M. Markou and S. Singh, “Novelty detection: a review—part 1: statistical approaches,” *Signal processing*, vol. 83, no. 12, pp. 2481–2497, 2003.
- [15] R. Yu and R. Wang, “Learning dynamical systems from data: An introduction to physics-guided deep learning,” *Proceedings of the National Academy of Sciences*, vol. 121, no. 27, p. e2311808121, 2024.
- [16] S. S. R. Hindupur, E. S. Lubana, T. Fel, and D. E. Ba, “Projecting assumptions: The duality between sparse autoencoders and concept geometry,” *CoRR*, vol. abs/2503.01822, 2025.
- [17] G. Grosso and M. Letizia, “Multiple testing for signal-agnostic searches for new physics with machine learning,” *Eur. Phys. J. C*, vol. 85, no. 1, p. 4, 2025.
- [18] M. M. Bronstein, J. Bruna, T. Cohen, and P. Veličković, “Geometric deep learning: Grids, groups, graphs, geodesics, and gauges,” *arXiv preprint arXiv:2104.13478*, 2021.
- [19] A. v. d. Oord, Y. Li, and O. Vinyals, “Representation learning with contrastive predictive coding,” *arXiv preprint arXiv:1807.03748*, 2018.
- [20] Y. Wang and M. I. Jordan, “Desiderata for representation learning: A causal perspective,” *arXiv preprint arXiv:2109.03795*, 2021.
- [21] S. Bright-Thonney, C. Reissel, G. Grosso, N. Woodward, K. Govorkova, A. Novak, S. E. Park, E. Moreno, and P. Harris, “Autoscidact: Automated scientific discovery through contrastive embedding and hypothesis testing,” *arXiv preprint arXiv:2510.21935*, 2025.
- [22] J. Liu, Z. Lin, S. Padhy, D. Tran, T. Bedrax Weiss, and B. Lakshminarayanan, “Simple and principled uncertainty estimation with deterministic deep learning via distance awareness,” *Advances in neural information processing systems*, vol. 33, pp. 7498–7512, 2020.
- [23] T. Reiss, N. Cohen, and Y. Hoshen, “No free lunch: The hazards of over-expressive representations in anomaly detection,” *arXiv preprint arXiv:2306.07284*, 2023.
- [24] S. Fort, J. Ren, and B. Lakshminarayanan, “Exploring the limits of out-of-distribution detection,” *Advances in neural information processing systems*, vol. 34, pp. 7068–7081, 2021.
- [25] Y. L. Li, D. Lu, P. Kirichenko, S. Qiu, T. G. Rudner, C. B. Bruss, and A. G. Wilson, “Out-of-distribution detection methods answer the wrong questions,” *arXiv preprint arXiv:2507.01831*, 2025.
- [26] G. Blanchard, G. Lee, and C. Scott, “Semi-supervised novelty detection,” *The Journal of Machine Learning Research*, vol. 11, pp. 2973–3009, 2010.
- [27] I. Steinwart, D. Hush, and C. Scovel, “A classification framework for anomaly detection,” *Journal of Machine Learning Research*, vol. 6, no. 2, 2005.
- [28] D. Lopez-Paz and M. Oquab, “Revisiting classifier two-sample tests,” in *5th International Conference on Learning Representations, ICLR 2017, Toulon, France, April 24–26, 2017, Conference Track Proceedings*, OpenReview.net.
- [29] X. Cheng and A. Cloninger, “Classification logit two-sample testing by neural networks for differentiating near manifold densities,” *IEEE Transactions on Information Theory*, vol. 68, no. 10, pp. 6631–6662, 2022.
- [30] K. Lee, K. Lee, H. Lee, and J. Shin, “A simple unified framework for detecting out-of-distribution samples and adversarial attacks,” *Advances in neural information processing systems*, vol. 31, 2018.
- [31] R. Chalapathy, A. K. Menon, and S. Chawla, “Anomaly detection using one-class neural networks,” *arXiv preprint arXiv:1802.06360*, 2018.
- [32] L. Ruff, R. Vandermeulen, N. Goernitz, L. Deecke, S. A. Siddiqui, A. Binder, E. Müller, and M. Kloft, “Deep one-class classification,” in *Proceedings of the 35th International Conference on Machine Learning (J. Dy and A. Krause, eds.)*, vol. 80 of *Proceedings of Machine Learning Research*, pp. 4393–4402, PMLR, 10–15 Jul 2018.
- [33] G. Grosso, M. Letizia, M. Pierini, and A. Wulzer, “Goodness of fit by Neyman-Pearson testing,” 5 2023.
- [34] R. T. D’Agnolo, G. Grosso, M. Pierini, A. Wulzer, and M. Zanetti, “Learning multivariate new physics,” *Eur. Phys. J. C*, vol. 81, no. 1, p. 89, 2021.
- [35] M. Letizia, G. Losapio, M. Rando, G. Grosso, A. Wulzer, M. Pierini, M. Zanetti, and L. Rosasco, “Learning new physics efficiently with nonparametric methods,” *Eur. Phys. J. C*, vol. 82, no. 10, p. 879, 2022.
- [36] R. Barlow, “Extended maximum likelihood,” *Nuclear Instruments and Methods in Physics Research Section A: Accelerators, Spectrometers, Detectors and Associated Equipment*, vol. 297, no. 3, pp. 496–506, 1990.
- [37] R. T. D’Agnolo and A. Wulzer, “Learning New Physics from a Machine,” *Phys. Rev. D*, vol. 99, no. 1, p. 015014, 2019.
- [38] G. Grosso, N. Lai, M. Letizia, J. Pazzini, M. Rando, L. Rosasco, A. Wulzer, and M. Zanetti, “Fast kernel methods for Data Quality Monitoring as a goodness-of-fit test,” *Machine Learning: Science and Technology*, vol. 4, no. 3, p. 035029, 2023.
- [39] S. Grossi, M. Letizia, and R. Torre, “Refereeing the referees: evaluating two-sample tests for validating generators in precision sciences,” *Mach. Learn. Sci. Tech.*, vol. 6, no. 1, p. 015052, 2025.
- [40] J. H. Friedman and L. C. Rafsky, “Multivariate generalizations of the wald-wolfowitz and smirnov two-sample tests,” *The Annals of Statistics*, vol. 7, no. 4, pp. 697–717, 1979.
- [41] J. H. Friedman and L. C. Rafsky, “Multivariate generalizations of the wald-wolfowitz and smirnov two-sample tests,” *The Annals of Statistics*, vol. 7, no. 4, pp. 697–717, 1979.
- [42] A. Gretton, K. M. Borgwardt, M. J. Rasch, B. Schölkopf, and A. Smola, “A kernel two-sample test,” *Journal of Machine Learning Research*, vol. 13, no. 25, pp. 723–773, 2012.
- [43] A. Chatalic, M. Letizia, N. Schreuder, and L. Rosasco, “An efficient permutation-based kernel two-sample test,” *arXiv preprint arXiv:2502.13570*, 2025.
- [44] P. R. Gerber, T. Jiang, Y. Polyanskiy, and R. Sun, “Kernel-based tests for likelihood-free hypothesis testing,” *Advances in Neural Information Processing Systems*, vol. 36, pp. 15680–15715, 2023.
- [45] P. Chakravarti, M. Kuusela, J. Lei, and L. Wasserman, “Model-Independent Detection of New Physics Signals Using Interpretable Semi-Supervised Classifier Tests,” 2 2021.
- [46] J. H. Friedman, “On multivariate goodness of fit and two sample testing,” *eConf*, vol. C030908, p. THPD002, 2003.
- [47] A. F. Agarap, “Deep learning using rectified linear units (relu),” *arXiv preprint arXiv:1803.08375*, 2018.
- [48] D. Fisch, A. Hofmann, and B. Sick, “On the versatility of radial basis function neural networks: A case study in the field of intrusion detection,” *Information Sciences*, vol. 180, no. 12, pp. 2421–2439, 2010.
- [49] M. Lau, I. Seck, A. P. Meliopoulos, W. Lee, and E. Ndiaye, “Revisiting non-separable binary classification and its applications in anomaly detection,” *arXiv preprint arXiv:2312.01541*, 2023.
- [50] C. J. Rozell, D. H. Johnson, R. G. Baraniuk, and B. A. Olshausen, “Sparse coding via thresholding and local competition in neural circuits,” *Neural computation*, vol. 20, no. 10, pp. 2526–2563, 2008.
- [51] S. Nowlan, “Maximum likelihood competitive learning,” in *Advances in Neural Information Processing Systems* (D. Touretzky, ed.), vol. 2, Morgan-Kaufmann, 1989.
- [52] T. Hoefler, D. Alistarh, T. Ben-Nun, N. Dryden, and A. Peste, “Sparsity in deep learning: Pruning and growth for efficient inference and training in neural networks,” *Journal of Machine Learning Research*, vol. 22, no. 241, pp. 1–124, 2021.
- [53] S. M. Omohundro, “Efficient algorithms with neural network behavior,” *Complex Systems*, vol. 1, no. 2, pp. 273–347, 1987.
- [54] D. S. Broomhead and D. Lowe, “Multivariable functional interpolation and adaptive networks,” *Complex Syst.*, vol. 2, 1988.
- [55] J. Park and I. W. Sandberg, “Universal approximation using radial-basis-function networks,” *Neural Computation*, vol. 3, no. 2, pp. 246–257, 1991.
- [56] T. Poggio and F. Girosi, “Regularization algorithms for learning that are equivalent to multilayer networks,” *Science*, vol. 247, no. 4945, pp. 978–982, 1990.
- [57] J. Moody and C. J. Darken, “Fast learning in networks of locally-tuned processing units,” *Neural computation*, vol. 1, no. 2, pp. 281–294, 1989.

- [58] Y. LeCun, S. Chopra, R. Hadsell, M. Ranzato, F. Huang, *et al.*, “A tutorial on energy-based learning,” *Predicting structured data*, vol. 1, no. 0, 2006.
- [59] W. Grathwohl, K.-C. Wang, J.-H. Jacobsen, D. Duvenaud, M. Norouzi, and K. Swersky, “Your classifier is secretly an energy based model and you should treat it like one,” *arXiv preprint arXiv:1912.03263*, 2019.
- [60] J. Moody, “Fast learning in multi-resolution hierarchies,” *Advances in neural information processing systems*, vol. 1, 1988.
- [61] J. A. Freeman and D. Saad, “Dynamics of on-line learning in radial basis function networks,” *Physical Review E*, vol. 56, no. 1, p. 907, 1997.
- [62] G. Meanti, L. Carratino, L. Rosasco, and A. Rudi, “Kernel methods through the roof: handling billions of points efficiently,” in *Advances in Neural Information Processing Systems 32*, 2020.
- [63] A. Gretton, K. Borgwardt, M. Rasch, B. Schölkopf, and A. Smola, “A kernel method for the two-sample-problem,” in *Advances in Neural Information Processing Systems (B. Schölkopf, J. Platt, and T. Hoffman, eds.)*, vol. 19, MIT Press, 2006.
- [64] W. Jitkrittum, Z. Szabó, K. Chwialkowski, and A. Gretton, “Interpretable distribution features with maximum testing power,” *arXiv preprint arXiv:1605.06796*, 2016.
- [65] J. M. Kübler, W. Jitkrittum, B. Schölkopf, and K. Muandet, “A witness two-sample test,” *arXiv preprint arXiv:2102.05573v3*, 2022.
- [66] J. M. Kübler, V. Stimper, S. Buchholz, K. Muandet, and B. Schölkopf, “Automl two-sample test,” *arXiv preprint arXiv:2206.08843v3*, 2023.
- [67] F. Biggs, A. Schrab, and A. Gretton, “Mmd-fuse: learning and combining kernels for two-sample testing without data splitting,” in *Proceedings of the 37th International Conference on Neural Information Processing Systems, NIPS ’23*, (Red Hook, NY, USA), Curran Associates Inc., 2023.
- [68] A. Schrab, I. Kim, M. Albert, B. Laurent, B. Guedj, and A. Gretton, “Mmd aggregated two-sample test,” *J. Mach. Learn. Res.*, vol. 24, Jan. 2023.
- [69] D. Amodei, C. Olah, J. Steinhardt, P. Christiano, J. Schulman, and D. Mané, “Concrete problems in ai safety,” *arXiv preprint arXiv:1606.06565*, 2016.
- [70] J. Yang, P. Wang, D. Zou, Z. Zhou, K. Ding, W. Peng, H. Wang, G. Chen, B. Li, Y. Sun, X. Du, K. Zhou, W. Zhang, D. Hendrycks, Y. Li, and Z. Liu, “OpenOOD: Benchmarking generalized out-of-distribution detection,” in *Advances in Neural Information Processing Systems 35: Datasets and Benchmarks Track (NeurIPS 2022)*, 2022.
- [71] O. Russakovsky, J. Deng, H. Su, J. Krause, S. Satheesh, S. Ma, Z. Huang, A. Karpathy, A. Khosla, M. Bernstein, A. C. Berg, and L. Fei-Fei, “ImageNet Large Scale Visual Recognition Challenge,” *International Journal of Computer Vision (IJCV)*, vol. 115, no. 3, pp. 211–252, 2015.
- [72] M. Cimpoi, S. Maji, I. Kokkinos, S. Mohamed, and A. Vedaldi, “Describing textures in the wild,” in *Proceedings of the IEEE conference on computer vision and pattern recognition*, pp. 3606–3613, 2014.
- [73] AI@Meta, “Llama 3 Model Card,” 2024.
- [74] N. Reimers and I. Gurevych, “Sentence-bert: Sentence embeddings using siamese bert-networks,” in *Proceedings of the 2019 Conference on Empirical Methods in Natural Language Processing*, Association for Computational Linguistics, 11 2019.
- [75] A. Krizhevsky, G. Hinton, *et al.*, “Learning multiple layers of features from tiny images,” 2009.
- [76] P. Nakkiran, B. Neyshabur, and H. Sedghi, “The deep bootstrap framework: Good online learners are good offline generalizers,” *arXiv preprint arXiv:2010.08127*, 2020.
- [77] J. Ho, A. Jain, and P. Abbeel, “Denoising diffusion probabilistic models,” *Advances in neural information processing systems*, vol. 33, pp. 6840–6851, 2020.
- [78] Z. Li, Y. Zhu, and M. Van Leeuwen, “A survey on explainable anomaly detection,” *ACM Transactions on Knowledge Discovery from Data*, vol. 18, no. 1, pp. 1–54, 2023.
- [79] I. Higgins, D. Amos, D. Pfau, S. Racaniere, L. Matthey, D. Rezende, and A. Lerchner, “Towards a definition of disentangled representations,” *arXiv preprint arXiv:1812.02230*, 2018.
- [80] N. Elhage, T. Hume, C. Olsson, N. Schiefer, T. Henighan, S. Kravec, Z. Hatfield-Dodds, R. Lasenby, D. Drain, C. Chen, *et al.*, “Toy models of superposition,” *arXiv preprint arXiv:2209.10652*, 2022.
- [81] D. Klindt, C. O’Neill, P. Reizinger, H. Maurer, and N. Miolane, “From superposition to sparse codes: interpretable representations in neural networks,” *arXiv preprint arXiv:2503.01824*, 2025.
- [82] H. Cunningham, A. Ewart, L. Riggs, R. Huben, and L. Sharkey, “Sparse autoencoders find highly interpretable features in language models,” *arXiv preprint arXiv:2309.08600*, 2023.
- [83] J. Colin, L. Goetschalckx, T. Fel, V. Boutin, J. Gopal, T. Serre, and N. Oliver, “Local vs distributed representations: What is the right basis for interpretability?,” *arXiv preprint arXiv:2411.03993*, 2024.
- [84] L. Sharkey, B. Chughtai, J. Batson, J. Lindsey, J. Wu, L. Bushnaq, N. Goldowsky-Dill, S. Heimersheim, A. Ortega, J. Bloom, *et al.*, “Open problems in mechanistic interpretability,” *arXiv preprint arXiv:2501.16496*, 2025.
- [85] A. Lin and D. E. Ba, “How to train your falcon: Learning log-concave densities with energy-based neural networks,” in *Fifth Symposium on Advances in Approximate Bayesian Inference*, 2023.
- [86] C.-K. Yeh, J. Kim, I. E.-H. Yen, and P. K. Ravikumar, “Representer point selection for explaining deep neural networks,” *Advances in neural information processing systems*, vol. 31, 2018.
- [87] P. J. Huber, “A robust version of the probability ratio test,” *The Annals of Mathematical Statistics*, vol. 36, no. 6, pp. 1753–1758, 1965.
- [88] G. Grosso, “Anomaly-aware summary statistic from data batches,” *JHEP*, vol. 12, p. 093, 2024.
- [89] R. Cheng and M. Stephens, “A goodness-of-fit test using moran’s statistic with estimated parameters,” *Biometrika*, vol. 76, no. 2, pp. 385–392, 1989.
- [90] J. Aasi *et al.*, “Advanced LIGO,” *Class. Quant. Grav.*, vol. 32, p. 074001, 2015.
- [91] LIGO Scientific, “The O3a Data Release,” Apr. 2021.
- [92] LIGO Scientific, “The O3b Data Release,” Nov. 2021.
- [93] E. Marx *et al.*, “Machine-learning pipeline for real-time detection of gravitational waves from compact binary coalescences,” *Phys. Rev. D*, vol. 111, no. 4, p. 042010, 2025.
- [94] H. Qu, C. Li, and S. Qian, “Jetclass: A large-scale dataset for deep learning in jet physics,” June 2022.
- [95] H. Qu, C. Li, and S. Qian, “Particle Transformer for Jet Tagging,” 2 2022.
- [96] G. Montejo-Kovacevich, E. van der Heijden, N. Nadeau, and C. Jiggins, “Cambridge butterfly wing collection batch 10,” Nov. 2020.
- [97] P. A. Salazar, N. Nadeau, G. Montejo-Kovacevich, and C. Jiggins, “Sheffield butterfly wing collection - Patricio Salazar, Nicola Nadeau, Ikiam broods batch 1 and 2,” Nov. 2020.
- [98] G. Montejo-Kovacevich, C. Jiggins, and I. Warren, “Cambridge butterfly wing collection batch 2,” May 2019.
- [99] C. Jiggins, G. Montejo-Kovacevich, I. Warren, and E. Wiltshire, “Cambridge butterfly wing collection batch 3,” May 2019.
- [100] G. Montejo-Kovacevich, C. Jiggins, I. Warren, and E. Wiltshire, “Cambridge butterfly wing collection batch 5,” May 2019.
- [101] I. Warren and C. Jiggins, “Miscellaneous Heliconius wing photographs (2001-2019) Part 1,” Feb. 2019.
- [102] I. Warren and C. Jiggins, “Miscellaneous Heliconius wing photographs (2001-2019) Part 3,” Feb. 2019.
- [103] G. Montejo-Kovacevich, C. Jiggins, I. Warren, and E. Wiltshire, “Cambridge butterfly wing collection batch 6,” May 2019.
- [104] C. Jiggins and I. Warren, “Cambridge butterfly wing collection - Chris Jiggins 2001/2 broods batch 1,” Jan. 2019.
- [105] C. Jiggins and I. Warren, “Cambridge butterfly wing collection - Chris Jiggins 2001/2 broods batch 2,” Jan. 2019.
- [106] J. I. Meier, P. Salazar, G. Montejo-Kovacevich, I. Warren, and C. Jiggins, “Cambridge butterfly wing collection - Patricio Salazar PhD wild specimens batch 3,” Oct. 2020.
- [107] G. Montejo-Kovacevich, C. Jiggins, and I. Warren, “Cambridge butterfly wing collection batch 1- version 2,” May 2019.
- [108] G. Montejo-Kovacevich, C. Jiggins, I. Warren, C. Salazar, M. Elias, I. Gavins, E. Wiltshire, S. Montgomery, and O. McMillan, “Cambridge and collaborators butterfly wing collection batch 10,” May 2019.

- [109] P. Salazar, G. Montejo-Kovacevich, I. Warren, and C. Jiggins, "Cambridge butterfly wing collection - Patricio Salazar PhD wild and bred specimens batch 1," Dec. 2018.
- [110] G. Montejo-Kovacevich, C. Jiggins, I. Warren, and E. Wiltshire, "Cambridge butterfly wing collection batch 7," May 2019.
- [111] P. Salazar, G. Montejo-Kovacevich, I. Warren, and C. Jiggins, "Cambridge butterfly wing collection - Patricio Salazar PhD wild and bred specimens batch 2," Jan. 2019.
- [112] E. Pinheiro de Castro, C. Jiggins, K. Lucas da Silva-Brandão, A. Victor Lucci Freitas, M. Zikan Cardoso, E. Van Der Heijden, J. Meier, and I. Warren, "Brazilian Butterflies Collected December 2020 to January 2021," Feb. 2022.
- [113] G. Montejo-Kovacevich, C. Jiggins, I. Warren, and E. Wiltshire, "Cambridge butterfly wing collection batch 8," May 2019.
- [114] G. Montejo-Kovacevich, C. Jiggins, I. Warren, E. Wiltshire, and I. Gavins, "Cambridge butterfly wing collection batch 9," May 2019.
- [115] G. Montejo-Kovacevich, E. van der Heijden, and C. Jiggins, "Cambridge butterfly collection - GMK Broods I kiam 2018," Nov. 2020.
- [116] G. Montejo-Kovacevich, Q. Paynter, and A. Ghane, "Heliconius erato cyrba, Cook Islands (New Zealand) 2016, 2019, 2021," Sept. 2021.
- [117] I. Warren and C. Jiggins, "Miscellaneous Heliconius wing photographs (2001-2019) Part 2," Feb. 2019.
- [118] C. Salazar, G. Montejo-Kovacevich, C. Jiggins, I. Warren, and I. Gavins, "Camilo Salazar and Cambridge butterfly wing collection batch 1," May 2019.
- [119] A. Mattila, C. Jiggins, and I. Warren, "University of Helsinki butterfly collection - Anniina Mattila bred specimens," Feb. 2019.
- [120] D. Dowson and B. Landau, "The fréchet distance between multivariate normal distributions," *Journal of multivariate analysis*, vol. 12, no. 3, pp. 450–455, 1982.